CHALMERS
UNIVERSITY OF TECHNOLOGY

A method for modelling arbitrarily shaped delamination fronts with large and distorted elements

Engineering Fracture Mechanics 306 (2024) 110193

Contents lists available at ScienceDirect

Engineering Fracture Mechanics

journal homepage: www.elsevier.com/locate/engfracmech

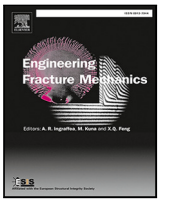

A method for modelling arbitrarily shaped delamination fronts with large and distorted elements

Pierre M. Daniel [a,b,*], Johannes Främby [c], Martin Fagerström [d], Pere Maimí [b]

[a] Btech[c] - Barcelona Technical Center S.L., Calle Juan de la Cierva N° 2, 08760 Martorell, Spain
[b] AMADE, Mechanical Engineering and Industrial Construction Department, University of Girona, Carrer Universitat de Girona 4, E-17003 Girona, Spain
[c] DYNAmore Nordic AB, Gothenburg, Sweden
[d] Department of Industrial and Materials Science, Division on Material and Computational Mechanics, Chalmers University of Technology, Gothenburg, Sweden

ARTICLE INFO

Keywords:
Delamination
Cohesive law
Energy release rate
Virtual crack closure technique
Efficient modelling

ABSTRACT

The simulation of delamination in layered composites is currently limited for large structures. Typically, the use of Cohesive Zone Modelling leads to a requirement of keeping the elements smaller than 1.0 mm. As an alternative, this article presents an Energy Release Rate-based cohesive method enabling the use of elements significantly larger (up to 5 mm). A novel algorithm is presented to use the Virtual Crack Closure Technique with distorted elements not aligned with the delamination front. When the propagation criterion is met, a cohesive law is introduced to model the progressive crack growth along the newly created crack surface, ensuring to dissipate the correct amount of energy. The method is validated for different propagation tests. Notably, Double Cantilever Beam and End-Notched Flexure tests are accurately modelled with large and distorted elements. Finally, a partially reinforced DCB test demonstrates the ability of the method in representing an evolving delamination front.

1. Introduction

In a context of vehicle structural weight reduction driven by the need to reduce energy consumption, the automotive, railway and aerospace industries are expected to further increase their use of lightweight composite materials such as Fibre-Reinforced Polymers (FRPs). During the design phase, the development teams rely on numerical simulation to assess the mechanical behaviour of the structure. In the case of layered FRPs, the modelling of delamination is necessary as it is one of the main damage mechanisms. However, the computational cost of available methods is a critical limitation for large structure applications.

Cohesive Zone Modelling (CZM) is currently the preferred solution for the numerical modelling of delamination. A traction–separation law is introduced at the layer interfaces prone to delamination to represent the Fracture Process Zone (FPZ) [1,2]. Consequently, the mesh must be smaller than the FPZ [3]. This mesh size requirement becomes restrictive in the case of FRPs due to the small FPZ of the delamination interface, typically smaller than 1 mm. Additionally, having at least 3 cohesive elements in the FPZ is recommended in the literature [3]. Finally, the initiation of propagation is based on the interface stress measured by introducing an artificial stiffness between layers. This stiffness must be sufficiently high such that the added artificial compliance is negligible. By doing so, it results in small stable time steps when using solvers based on explicit time integration. These computational limitations lead to the impracticality of the CZM for large structures, especially under dynamic loads.

* Corresponding author at: AMADE, Mechanical Engineering and Industrial Construction Department, University of Girona, Carrer Universitat de Girona 4, E-17003 Girona, Spain.
E-mail address: pdaniel@btechc.com (P.M. Daniel).

https://doi.org/10.1016/j.engfracmech.2024.110193
Received 27 February 2024; Received in revised form 3 May 2024; Accepted 29 May 2024
Available online 6 June 2024

Several works have been conducted to alleviate the computational cost induced by CZM. To some extent, the interface strength can be reduced to artificially increase the size of the FPZ [3]. This workaround is limited as the peak force and damage initiation rapidly become inaccurate. Another improvement lies in optimising the cohesive element integration scheme, allowing for fewer elements in the FPZ [4]. Ultimately, these solutions are still limited by the size of the FPZ. To overcome this limit, recent works use higher-order cohesive formulations to better capture the displacement field around the crack tip [5,6]. These promising formulations allow for cohesive elements larger than the FPZ. However, they require compatible surrounding elements and have not yet been validated further than beam-like geometries.

Another well-known approach to assess delamination propagation is the estimation of the Energy Release Rate (ERR). The most used methods being the J-integral [7–9] and the Virtual Crack Closure Technique (VCCT) [10,11]. When they are not based on underlying CZM [12], the ERR methods are usually based on the assumptions of Linear Elastic Fracture Mechanics (LEFM). That is, the interface is brittle such that the FPZ is small compared to the existing crack. The ERR evaluation does not necessarily rely on the interface stress to predict the crack growth. Therefore, under the correct conditions, some ERR methods can be applied to larger elements. This has been shown in the case of the VCCT [13–15].

Using the VCCT, the ERR is evaluated by means of the crack tip forces, the openings behind the crack tip and the area to be opened [11]. These quantities are evaluated at nodes of the underlying mesh, which is assumed orthogonal with respect to the crack front. Therefore, considerations are needed when the crack front is not aligned with the mesh, or when the elements are distorted. In an effort to resolve this mesh dependency, a range of algorithms have been proposed. Initial works focused specifically on the effect of mesh distortion [16,17]. Conversely, the algorithm from Xie et al. [18,19] considered a regular mesh but an arbitrarily shaped delamination front. Together with other relevant methods [14,20], the algorithm by Xie et al. has been compared recently for a radial crack in a regular squared mesh by Wu et al. [21]. The algorithm by Xie et al. has been further developed by Liu et al. [22,23] and later on extended to distorted mesh by Marjanović et al. [24].

The estimation of the ERR by the VCCT predicts the crack propagation initiation but does not actually model this propagation. That is, when the ERR reaches the fracture toughness G_c of the material, the crack front is updated assuming to have suddenly grown along the entire newly created crack surface. As a result, the method does not dissipate the energy necessary to open this crack surface. For this reason, instabilities are observed when using large elements [13,25]. Additionally, the delamination is observed to grow faster when the mesh is not aligned with the crack front [26,27]. The increased growth speed is caused by overestimating the ERR at sharp corners formed by the discretised front [25,26,28]. These ERR concentrations are due to higher crack tip forces appearing at corner nodes.

To solve these issues, Mabson et al. [29,30] have proposed to progressively release the constraint at the crack front once the VCCT criterion is met. Thus, absorbing the energy corresponding to the area being opened and alleviating the unrealistic ERR concentrations. The method has latter been extended to arbitrary crack fronts in regular mesh by De Carvalho et al. [28,31,32]. However, the ability of such approach in modelling an evolving delamination front shape with large and distorted elements is yet to be demonstrated.

Aiming to develop a similar solution to model delamination propagation with large elements in dynamic cases, the present authors have published a method called ERR-Cohesive [33]. Once the VCCT criterion is met, a cohesive law is introduced to model the progressive growth of the crack along the newly created crack surface. A novel damage formulation ensures to dissipate the correct amount of energy corresponding to the current mode-mixity. Additionally, the ERR-Cohesive method does not introduce any initial artificial stiffness at the layer interface. Promising results were obtained using large elements (2 mm to 8 mm) in standard propagation tests [33]. However, although dissimilar element lengths ahead and behind crack front have been resolved in this previous publication [33], the problem of an underlying distorted mesh representing an arbitrary shaped crack front has not been treated. Solving this issue is needed for a wider adoption of the method into the industry, where the mesh is distorted due to the geometrical complexity of the components.

The aim of the present work is to extend the ERR-Cohesive method to allow for arbitrarily shaped delamination front and large distorted elements. Starting from the VCCT and the cohesive formulation derived in the previous work [33], an algorithm is presented to define the crack front growth direction and the related quantities needed by the VCCT: force at the crack tip, opening behind the crack tip, area to be cracked and characteristic lengths on either sides of the crack tip.

The method is implemented in the frame of an adaptive user element [34,35] by means of a subroutine in the commercial solver LS-DYNA [36]. Various examples are presented as numerical validation. Double Cantilever Beam (DCB) and End-Notched Flexure (ENF) tests are simulated with distorted elements and meshes not aligned with the crack front. The method is used to model a square plate [37] where the unbonded area is transitioning from an initial rectangular shape to a steady state circular shape. Finally, the Reinforced-DCB test proposed by Carreras et al. [38], with an evolving shape of the delamination front, is modelled with a 1.8 mm and 5 mm mesh. The results show the accuracy of the method in predicting the growth of arbitrarily shaped delamination front as well as being compatible with distorted elements.

2. Model description

The ERR-Cohesive method adapted for arbitrarily shaped delamination fronts is presented in this section. Firstly, the necessary reminders are made on the ERR-Cohesive method presented in [33]. That is, the crack propagation criterion based on the VCCT, and the energy dissipation mechanism based on a cohesive law are detailed. Then, the novel adaptations made to account for arbitrarily shaped delamination fronts and distorted elements are described.

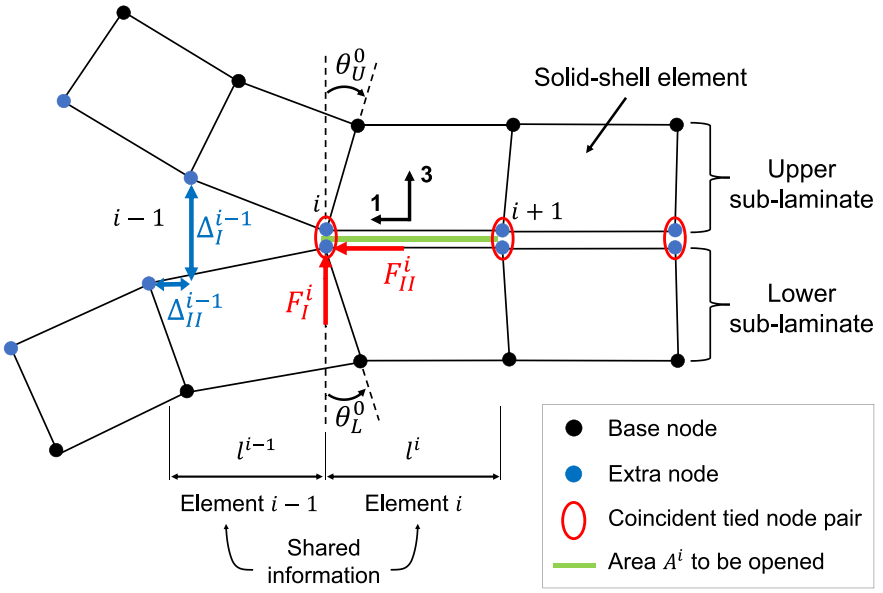

Fig. 1. Crack tip configuration used in the present method for the ERR evaluation by the VCCT. This crack tip configuration simplified to a 2D cross-section can be used when the mesh is aligned with the crack growth direction. Each element is composed of 8 base nodes and 8 extra nodes to represent the crack interface. The necessary information (e.g. openings and internal forces) is shared among neighbouring elements.

2.1. Framework

The present model is part of an adaptive modelling approach [34,35]. The simulation starts in an unrefined state with the entire laminate being represented by a single through-the-thickness linear solid-shell element defined by 8 base nodes. In order to detect delamination risk at unrefined ply interfaces, a method has previously been developed to reliably recover the out-of-plane stress profiles of linear elements based on first-order shear deformation theory [39]. When a given refinement criterion is triggered, the model can – where necessary – be refined through the thickness to represent delamination cracks. This is achieved by adding 8 new nodes at the appropriate ply interface. The laminate is suitably split between the newly defined lower and upper elements.

In the present work, a delamination crack is assumed to have initiated. Therefore, only the final state of the adaptive procedure (where the interface is already refined) is used. In order to model a bonded interface, the nodes at the enriched interface are coincident in space and tied together by imposing equal acceleration on both nodes [33,34]. If a cracked interface is to be modelled, the refined nodes are set free from each other, and a frictionless penalty contact is introduced. An illustration of the initial state of refinement for the present study is shown in Fig. 1, although simplified to a 2D cross-section.

2.2. Crack propagation criterion

The method aims to accurately model the propagation of the crack with large elements. The interface considered is assumed to be brittle, such that the assumption of LEFM can be applied. Furthermore, the FPZ is assumed to be smaller than the element length. Therefore, the interface stresses at the crack tip would not be accurate and an ERR-based propagation criterion is preferred: the crack grows when the ERR reaches the fracture toughness G_c of the interface.

The evaluation of the ERR is made by means of the VCCT. In addition to the original crack closure method by Irwin [40], the VCCT proposed by Rybicki et al. [10] assumes a self-similar crack propagation which allows for an evaluation of the ERR in a single analysis. It results in a straightforward application to finite element analysis and has proven to be accurate with large elements [13–15,33]. The mode specific ERRs, G_α for mode α ($\alpha = I, II, III$), are evaluated by measuring the force F_α^i at the crack tip node pair i, the opening Δ_α^{i-1} at the node pair $i-1$ behind the crack tip and the area A^i to be opened by the releasing of the constraint at node pair i:

$$G_I = \frac{1}{2A^i} F_I^i \left\langle \Delta_I^{i-1} \right\rangle c_I^i, \tag{1a}$$

$$G_{II} = \frac{1}{2A^i} F_{II}^i \Delta_{II}^{i-1} c_{II}^i, \tag{1b}$$

$$G_{III} = \frac{1}{2A^i} F_{III}^i \Delta_{III}^{i-1} c_{III}^i, \tag{1c}$$

where $\langle\rangle$ are the Macaulay brackets defined as $\langle x \rangle = \frac{1}{2}(x + |x|)$, and c_α^i is a shape correction factor for mode α defined below. The force F_α^i responsible for keeping the nodes coincident can be computed by knowing the contributions from the elements below (or above) the interface at the node pair i [33]. The force and the opening are expressed in the crack front local coordinate system shown in Fig. 1.

For the self-similar assumption to be respected, the distance to the crack tip l^{i-1} from which the opening Δ^{i-1} is measured should be equal to the increase in crack length l^i resulting from the releasing of node pair i. To allow for dissimilar element length, the following correction factors are used in Eq. (1):

$$c_I^i = \frac{l^i}{\Delta_I^{i-1}}\theta^0(1-C) + C^2, \tag{2a}$$

$$c_{II}^i = C, \tag{2b}$$

$$c_{III}^i = C, \tag{2c}$$

where $C = \frac{l^i}{l^{i-1}}$ and θ^0 is the crack tip opening angle. θ^0 is approximated as $\theta^0 = \theta_U^0 + \theta_L^0$ where θ_U^0 and θ_L^0 are the angles formed between the sub-laminate cross section and the crack tip normal, respectively, for the upper and lower arm, see Fig. 1. For more details on the derivation of these corrections factor, refer to [33].

The total ERR G_T is calculated as the sum of the modal ERRs:

$$G_T = G_I + G_{II} + G_{III}. \tag{3}$$

The critical fracture toughness G_c is defined using the Benzeggagh–Kenane equation [41] by means of the pure mode I fracture toughness G_{Ic} and assuming that mode II and mode III have the same fracture toughness G_{IIc},

$$G_c = G_{Ic} + \left[G_{IIc} - G_{Ic}\right] B^\eta, \tag{4}$$

where B is the mixed-mode ratio defined as

$$B = \frac{G_{II} + G_{III}}{G_T}, \tag{5}$$

and the exponent η is a parameter to be determined experimentally.

Following the fracture mechanics growth criterion, when the total ERR G_T exceeds the corresponding fracture toughness G_c of the interface, the crack propagation initiates. To represent the progressive crack growth from node pair i to node pair $i+1$, the constraint keeping the node pair coincident is gradually released through the introduction of a cohesive law. This cohesive law ensures that the amount of energy AG_c corresponding to the opening surface will be dissipated.

2.3. Energy dissipation mechanism

The cohesive law needs to initiate with an initial non-zero traction force F_α^i. This force corresponds to the interface force needed to tie the node pair i at the moment the ERR propagation criterion is met. Below, the cohesive law is derived for any given node pair being released, the superscript i is dropped in the notation and the initial tying force F_α^i becomes F_α^0.

Recalling the derivations presented in [33], the interface force F_α^0 is degraded according to the cohesive law expressed as

$$F_I = \frac{\left|F_I^0\right|}{\Delta_I^{max}}(1-D)\left(\langle\Delta_I\rangle + \Delta_I^{offset}\right) - k_p\langle-\Delta_I\rangle, \tag{6a}$$

$$F_{II} = \frac{\left|F_{II}^0\right|}{\Delta_{II}^{max}}(1-D)\left(\Delta_{II} + \Delta_{II}^{offset}\right), \tag{6b}$$

$$F_{III} = \frac{\left|F_{III}^0\right|}{\Delta_{III}^{max}}(1-D)\left(\Delta_{III} + \Delta_{III}^{offset}\right), \tag{6c}$$

where k_p is a penalty contact stiffness, the damage variable D and the maximum opening Δ_α^{max} will be defined below, and Δ_α^{offset} is an opening offset introduced to avoid infinite initial stiffness. The opening offset is defined for a desired initial stiffness k_α^0 through

$$\Delta_\alpha^{offset} = \frac{F_\alpha^0}{k_\alpha^0}. \tag{7}$$

For unloading cases, the opening offset Δ_α^{offset} should be small to avoid unrealistic behaviours, refer to [33] for more details. Finally, the maximum opening in mode α is defined as

$$\Delta_I^{max} = \max_{\tau\in[0,t]}\left\langle\Delta_I(\tau) + \Delta_I^{offset}\right\rangle, \tag{8a}$$

$$\Delta_{II}^{max} = \max_{\tau\in[0,t]}\left|\Delta_{II}(\tau) + \Delta_{II}^{offset}\right|, \tag{8b}$$

$$\Delta_{III}^{max} = \max_{\tau\in[0,t]}\left|\Delta_{III}(\tau) + \Delta_{III}^{offset}\right|, \tag{8c}$$

where Δ_I^{max} is initialised to $|\Delta_I^{offset}|$ to account for cases where Δ_I^{offset} is negative. By defining the current stiffness in mode α as a function of the damage D and the maximum opening Δ_α^{max} such that

$$k_\alpha = \frac{\left|F_\alpha^0\right|}{\Delta_\alpha^{max}}(1-D), \tag{9}$$

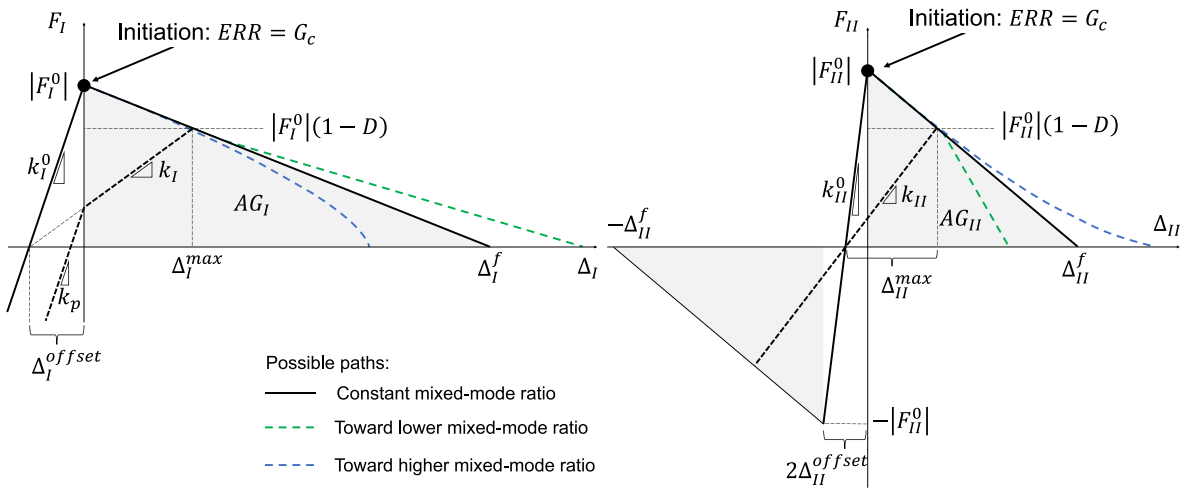

(a) Mode I representation. (b) Mode II representation.

Fig. 2. Force–opening representation of the cohesive law. The cohesive law is initiated with the forces F_I^0 and F_{II}^0 for which ERR = G_c. The mode III representation is not shown as it is analogous to mode II representation. The opening offset Δ_α^{offset} ensures the initial stiffness to have a finite value.

the cohesive law can also be expressed as

$$F_I = k_I \left(\langle \Delta_I \rangle + \Delta_I^{offset} \right) - k_p \langle -\Delta_I \rangle , \tag{10a}$$

$$F_{II} = k_{II} \left(\Delta_{II} + \Delta_{II}^{offset} \right) , \tag{10b}$$

$$F_{III} = k_{III} \left(\Delta_{III} + \Delta_{III}^{offset} \right) . \tag{10c}$$

The damage variable D is defined through the damage function d as

$$d = \frac{1}{2AG_c} \left(\left| F_I^0 \right| \langle \Delta_I^* \rangle + \left| F_{II}^0 \right| \langle \Delta_{II}^* \rangle + \left| F_{III}^0 \right| \langle \Delta_{III}^* \rangle \right) , \tag{11}$$

where Δ_α^* is the damage-driving opening which has to be adapted for the opening offset as

$$\Delta_I^* = \left\langle \Delta_I + \Delta_I^{offset} \right\rangle - \left| \Delta_I^{offset} \right| , \tag{12a}$$

$$\Delta_{II}^* = \left| \Delta_{II} + \Delta_{II}^{offset} \right| - \left| \Delta_{II}^{offset} \right| , \tag{12b}$$

$$\Delta_{III}^* = \left| \Delta_{III} + \Delta_{III}^{offset} \right| - \left| \Delta_{III}^{offset} \right| . \tag{12c}$$

The damage is ensured to be in the $[0, 1]$ interval by setting

$$D = \max_{\tau \in [0,t]} \left[\min\{1, d(\tau)\} \right] . \tag{13}$$

The function d can be expressed equivalently as

$$d = B_I \frac{\langle \Delta_I^* \rangle}{\left| \Delta_I^f \right|} + B_{II} \frac{\langle \Delta_{II}^* \rangle}{\left| \Delta_{II}^f \right|} + B_{III} \frac{\langle \Delta_{III}^* \rangle}{\left| \Delta_{III}^f \right|} . \tag{14}$$

Where $B_\alpha = \frac{G_\alpha}{G_T}$ is the mode-mixity obtained from the VCCT and Δ_α^f is the failure opening defined as the opening at which the energy AG_α would be consumed by linear softening in mode α,

$$\Delta_\alpha^f = \frac{2AG_\alpha}{F_\alpha^0} . \tag{15}$$

An illustration of the cohesive law is presented in Fig. 2. It is worth mentioning that the constitutive equations of the cohesive law are implemented in the local coordinates of the deformed interface, allowing for large displacement analysis. The energy AG_c to be dissipated is obtained from the area and mixed-mode ratio evaluated by the ERR. In that sense, AG_c is an input of the cohesive law and is kept constant during the node releasing. Although the force F_α^0 is degraded equally for the three modes, the damage D is a function of the openings. Therefore, the cohesive law does not impose the softening to be linear. In practice, linear softening is observed under constant mode-mixity. In the case of a sudden change to a lower mode-mixity, the bilinear law represented by the

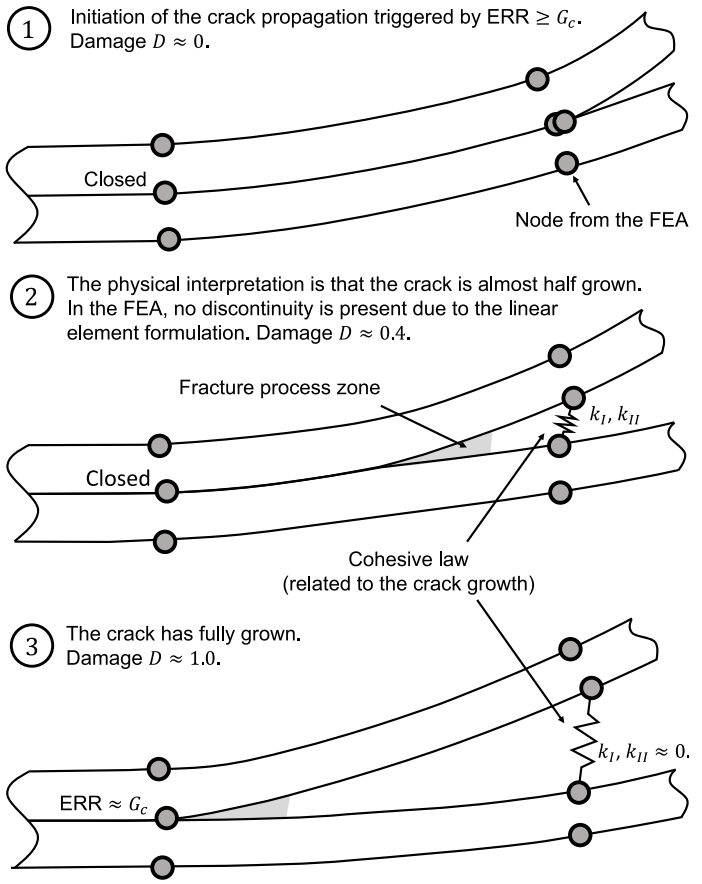

Fig. 3. Present crack propagation modelling. The crack propagation is triggered by the ERR estimation. A cohesive law is introduced to model the crack propagation along the newly created crack surface.

green line in Fig. 2 is an opening path allowed by the present formulation. Similarly, in the case of a progressive transition towards higher mixed mode ratio, the cohesive law could follow the blue line.

One of the motivations behind the damage function in Eq. (11) and Eq. (14) is that it ensures the input amount of energy AG_c to be dissipated for any monotonic paths that could be followed by the openings during the node releasing. More specifically, it has been demonstrated in [33], that the energy dissipated is proportional to the damage D such that

$$\mathcal{G} = AG_c D. \tag{16}$$

This equation leads to an interpretation of D as being the proportion of cracked area over the total area to be opened A. It should be reminded that the present method is aimed to be used with elements larger that the FPZ. Thus, the cohesive law represents a crack growing along the newly created crack surface, see Fig. 3.

The present cohesive law introduces a penalty stiffness, which can limit the stable time step in analysis with explicit integration scheme. However, a relatively low stiffness can typically be used for two reasons. First, the stiffness is localised at the crack front, avoiding general artificial compliance to be added to the model. Second, the impact of the chosen stiffness value is limited to unloading, as the cohesive law initiates at damage initiation, see Fig. 2. Ultimately, mass scaling could be used locally at the crack tip to ensure a convenient stable time step.

2.4. Interface damping

In addition to the constitutive model presented in [33], a mass proportional damping is introduced at the interface node pair during the progressive releasing. The use of interface damping allows to stabilise unrealistic local vibrations. It is extensively used in commercial software, especially for contact problems. In the present case, it has shown to reduce vibrations under unstable crack propagation. The damping is based on the relative velocity of the two interface nodes $\dot{\Delta}_\alpha$ and the damping coefficient c_{damp} through:

$$F_\alpha^{damp} = c_{damp}\dot{\Delta}_\alpha. \tag{17}$$

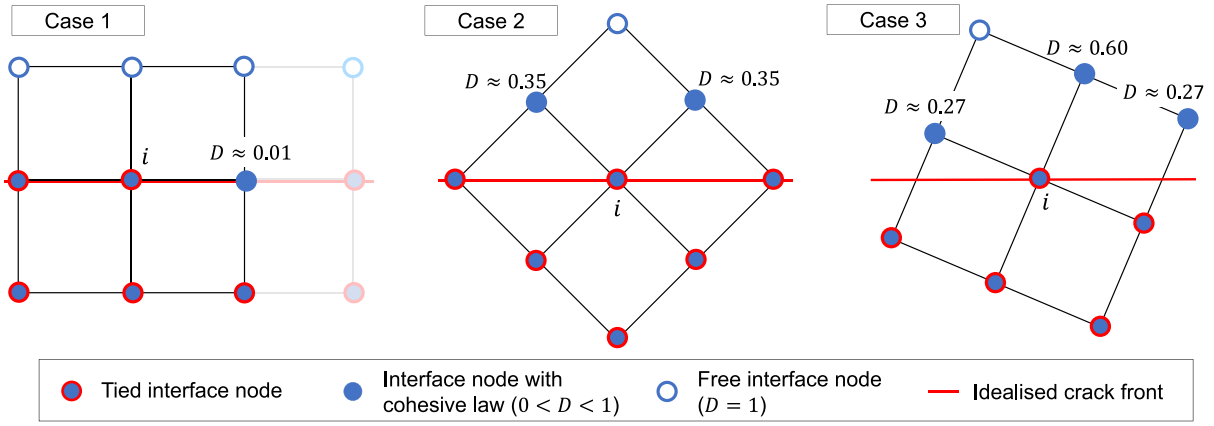

Fig. 4. Examples of regular mesh with different orientation with respect to the imposed crack front. The configurations are observed when the crack front reaches the node i. These cases illustrate the need to account for the damage D of the nearby nodes to define the crack front.

The damping coefficient is taken as 10% of the critical damping c_c calculated for a typical spring–mass system through

$$c_c = \frac{4}{b}\sqrt{m k_\alpha^0}, \tag{18}$$

where m is the effective mass of the node pair and b is a coefficient depending on the stiffness of the connected elements ($b = 1.2$ is considered here). The damping is present only while the cohesive law is acting on the node pair, it is removed when $D = 1$.

2.5. Arbitrarily shaped front

For the estimation of the ERR by the VCCT, the quantities appearing in Eq. (1) need to be evaluated. If a regular squared mesh oriented orthogonally with respect to the crack front is assumed, the evaluation is straightforward, see also Fig. 1. However, defining the necessary quantities is challenging when the underlying mesh is distorted and not aligned with the crack front. This applies to the following:

- The local coordinate system at node i defining the crack growth direction. The force F_α^i and opening Δ_α^{i-1} will be expressed in this coordinate system.
- The node $i-1$ from which the opening Δ_α^{i-1} is retrieved.
- The area A^i to be opened when releasing node i, according to the local shape of the crack front.
- The characteristic lengths ahead of the crack tip l^i and behind the crack tip l^{i-1}, needed for the correction factor c_α^i.

As explained in the introduction, several authors have proposed algorithms to solve this issue. Naturally, the algorithm proposed in this paper is largely inspired by these works. However, a particular focus is made on the compatibility with both a damage mechanism and distorted elements. The energy absorption mechanism removes the binary nature of the nodes being either closed or opened. Instead, some node pairs near the crack tip are partially released according to the cohesive law expressed in Eq. (6). It is worth mentioning that the algorithm is defined for 8-node solid-shell elements, 6-node elements (extruded triangles) are not considered.

Recalling that the FPZ is assumed to be much smaller than the element length, the crack front is reduced to a line. In the algorithm by De Carvalho et al. [32], the damage value is used to interpolate the crack front position along the element's edges orthogonal to the front. In the present case, where arbitrarily shaped fronts are expected to propagate in large and distorted elements, a linearly interpolated crack front based on the damage value would be poorly defined. Furthermore, it should be remembered that the method does not assume a crack growth direction a priori.

As an alternative approach, it is assumed that the crack front follows the element edges and diagonals. In addition, the relative distance of the partially released nodes to the crack front is assumed to be proportional to the damage D, as suggested by Eq. (16). A threshold value D_0 is defined to decide whether the partially released node should be considered for the current crack front. Therefore, nodes with a low damage value ($D < D_0$) are assumed to be part of the current crack front. Nodes with a higher damage value ($D > D_0$) are assumed to be far from the current crack front.

To motivate for the definition of a threshold value D_0, three different crack tip configuration examples are presented in Fig. 4. These examples present an idealised straight crack front growing in a DCB-like specimen, modelled with a regular mesh of different orientations. The node status and associated damage values are observed at the time the ERR reaches the critical value G_c at node

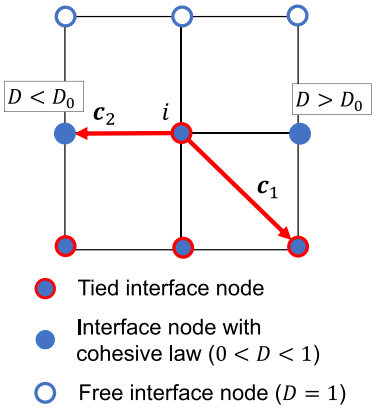

Fig. 5. Crack front centred around node i. Only the bottom nodes of the interface are represented. The nodes are either tied with their paired upper node (i.e. ERR< G_c), connected to their paired upper node by the cohesive law ($0 < D < 1$), or free ($D = 1$). To define the crack front, the nodes with $D < D_0$ are assumed to be bonded. The crack front is then defined by vectors $\boldsymbol{c}_1$ and $\boldsymbol{c}_2$ delimiting the bonded and free areas.

i. The presented examples are obtained with a 5 mm mesh for a specific specimen and DCB-like load case. However, the general observations have shown to stand when using the present solid-shell formulation and modelling configuration.

In case 1, when the crack front is aligned with the mesh, the crack front follows the element edges. Along the front, one node will open sooner than the others, typically due to its central position. However, the damage D at this node will remain low until the other nodes of the crack front open as well. In this case, it is clear that low values of D do not induce a change in the shape of the crack front. In practice, with distorted meshes and non-aligned edges, some nodes tend to accumulate damage faster than other in the same crack front. Depending on the degree of distortion, such cases can reach damage values higher than $D \approx 0.20$. In case 2, where the mesh is oriented at 45°, the crack front follows the diagonals of the elements. It is observed that the node i should open when some nodes behind the crack tip have a damage $D \approx 0.35$. These nodes are part of a preceding crack front and should not be considered for the current crack front. Finally, in case 3, with a mesh oriented at 22.5°, there is no clear crack front definition based on element edges and diagonals, However, it is observed that node i should open when some nodes behind the crack tip have a damage $D \approx 0.27$. For such cases, several crack front directions will be considered, as explained below.

These examples motivate for a value of D_0 roughly between 0.20 and 0.27. Namely, $D_0 = 0.25$ (corresponding to 25% of the energy dissipated), gives the best results in practice and is used in the present work. It is likely that the value of D_0 would need to be adapted when using another element formulation or modelling configuration. For a better assessment of the chosen value of D_0 regarding the sensitivity to mesh size and element distortion, refer to Section 3.

Considering a tied node i at the crack front (see Fig. 5), the crack front in its vicinity is defined by two vectors $\boldsymbol{c}_1$ and $\boldsymbol{c}_2$. Considering all neighbouring nodes in a counter-clockwise direction, $\boldsymbol{c}_1$ points from the tied node to another bonded node (i.e. tied or $D < D_0$) that is followed by a free node. Further, $\boldsymbol{c}_2$ points to the bonded node that is preceded by a free node.

Once the crack front is defined, the area A^i that will be opened by the releasing of node i can be estimated. A^i is used both for the evaluation of the ERR by the VCCT and for the cohesive law through the energy to be dissipated, $A^i G_c$. The way in which A^i is evaluated depends on the angle β from $\boldsymbol{c}_2$ to $\boldsymbol{c}_1$. A threshold value $\beta_0 = 150°$ is defined to differentiate between a convex crack front $\beta < \beta_0$, and a straight or concave crack front $\beta > \beta_0$. The value $\beta_0 = 150°$ is chosen sufficiently lower than 180° such that nearly straight crack fronts are still treated with the straight or concave front definition ($\beta > \beta_0$). At the same time, it is defined sufficiently larger than 135° to ensure that the case 3 of Fig. 7 is treated according to the convex front definition ($\beta_0 < \beta_0$). The area A^i is defined as follows:

- If $\beta > \beta_0$, it is assumed that the crack front is sufficiently well represented. The nodes pointed by vectors $\boldsymbol{c}_1$ and $\boldsymbol{c}_2$ are expected to open almost simultaneously with node i. In this case, A^i is defined by the polygon delimited by the points $\left(i, \mathrm{C}_2^1, \left(\mathrm{C}_2^2\right)_{\text{edge}}, \mathrm{E}_1, \ldots, \mathrm{E}_N, \left(\mathrm{C}_1^2\right)_{\text{edge}}, \mathrm{C}_1^1\right)$ as shown in the case 4 and 5 of Fig. 6. C_2^1 (equivalently C_1^1) is halfway along $\boldsymbol{c}_2$ ($\boldsymbol{c}_1$). The notation $(\bullet)_{\text{edge}}$ around C_2^2 (equivalently C_1^2) specifies that this point is included in the definition of the polygon only if $\boldsymbol{c}_2$ ($\boldsymbol{c}_1$) is along an element edge. In that case, C_2^2 (equivalently C_1^2) is the midpoint of the bonded edge opposite to $\boldsymbol{c}_2$ ($\boldsymbol{c}_1$). Finally, the nodes E_1 to E_N are the nodes, in the counter-clockwise direction, between $\boldsymbol{c}_2$ and $\boldsymbol{c}_1$ sharing an edge with node i.
- If $\beta < \beta_0$, it is assumed that the crack front is not well represented. The nodes pointed by $\boldsymbol{c}_1$ and $\boldsymbol{c}_2$ will not open at a time near the opening of node i. In this case, A^i is defined by the polygon delimited by the points $\left(i, \mathrm{C}_2^1, \mathrm{E}_1, \ldots, \mathrm{E}_N, \mathrm{C}_1^1\right)$ as shown

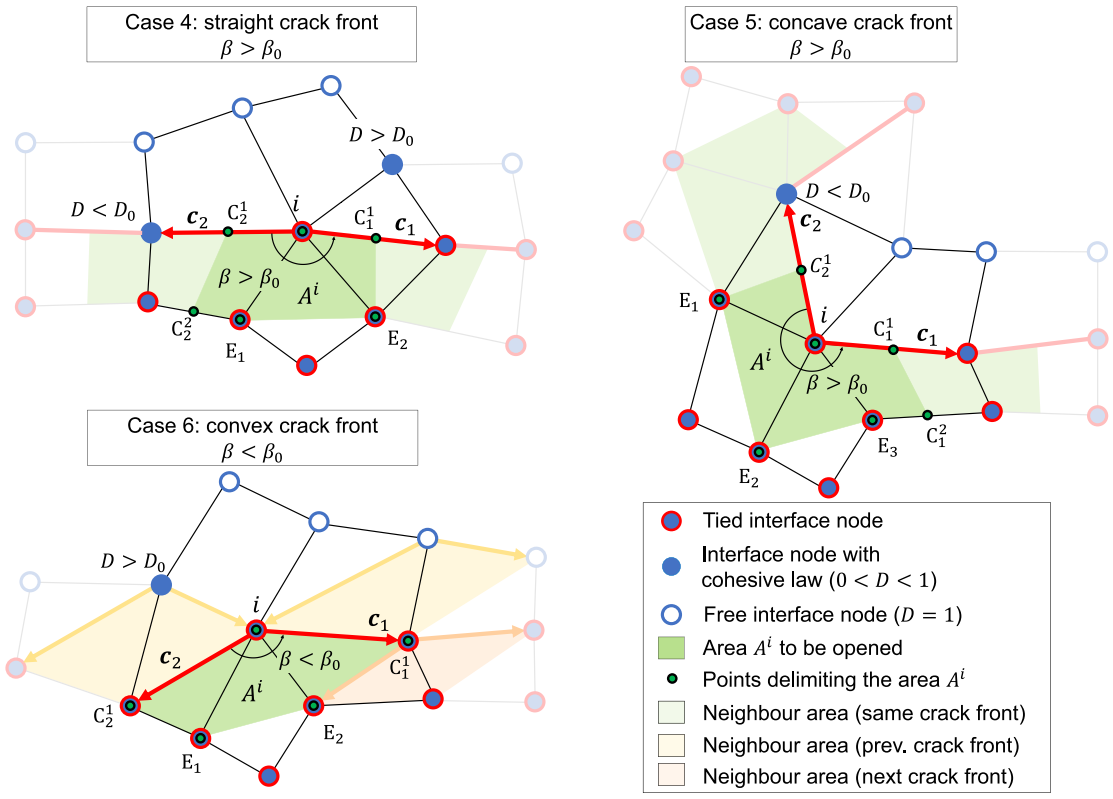

Fig. 6. General definition of the area A^i. The general definition applies when at least 4 consecutive nodes are bonded ($D < D_0$), starting in the counter-clockwise direction with the node pointed by $\boldsymbol{c}_2$ and ending with the node pointed by $\boldsymbol{c}_1$. The definition of A^i is different for the case $\beta > \beta_0$ and $\beta < \beta_0$ with $\beta_0 = 150°$. To show the continuity around the crack front, the area considered for the neighbouring nodes are also shown with transparency.

in the case 6 of Fig. 6. C_2^1 (equivalently C_1^1) is the node pointed by $\boldsymbol{c}_2$ ($\boldsymbol{c}_1$). The nodes E_1 to E_N have the same definition as in the $\beta > \beta_0$ case

In Fig. 6, the areas considered by the neighbouring nodes along the crack front are shown with transparency. In the convex crack front case, where the crack front is assumed to be poorly discretised, the neighbouring areas represent nodes which are considered to belong to the preceding or following state of the crack front. Under the assumptions of steady-state growth and limited distortion, the considered areas are continuous along the front and do not present overlap.

Before measuring the opening behind the crack front, it is necessary to define the crack growth direction. Following the self-similar growth assumption of the VCCT, the crack is assumed to grow orthogonally to the local delamination front:

- In the case where $\beta < \beta_0$, the crack front is poorly represented and three possible crack front directions are considered: $\boldsymbol{n}_1$, $\boldsymbol{n}_2$ and $\boldsymbol{n}_0$ (see the cases 3 and 6 in Fig. 7). The normalised vectors $\boldsymbol{n}_1$ and $\boldsymbol{n}_2$ are respectively orthogonal to $\boldsymbol{c}_1$ and $\boldsymbol{c}_2$. Then, $\boldsymbol{n}_0$ is defined through:

$$\boldsymbol{n}_0 = \frac{\boldsymbol{n}_1 + \boldsymbol{n}_2}{\|\boldsymbol{n}_1 + \boldsymbol{n}_2\|}. \tag{19}$$

- In the case where $\beta > \beta_0$, the crack front is assumed to be sufficiently well represented and only $\boldsymbol{n}_0$ is considered (see the cases 1, 2, 4 and 5 in Fig. 7).

For each considered growth direction, a local coordinate system is defined by the growth direction vector $\boldsymbol{n}_d$ ($d = 0, 1, 2$) and the normal to the interface plane. The vector tangent to the crack front being orthogonal to these two vectors. The opening is measured at the point $i - 1$ defined as the intersection between the perimeter edges of the neighbouring elements and the crack growth direction on the debonded side, see examples in Fig. 7. The opening Δ_α^{i-1} is calculated by subtracting the displacement of the upper and lower surface of the interface at point $i - 1$. The opening Δ_α^{i-1} and the force F_α^i are expressed in the local coordinate system of the considered growth direction, allowing to decompose mode I, II and III contributions according to Eq. (1).

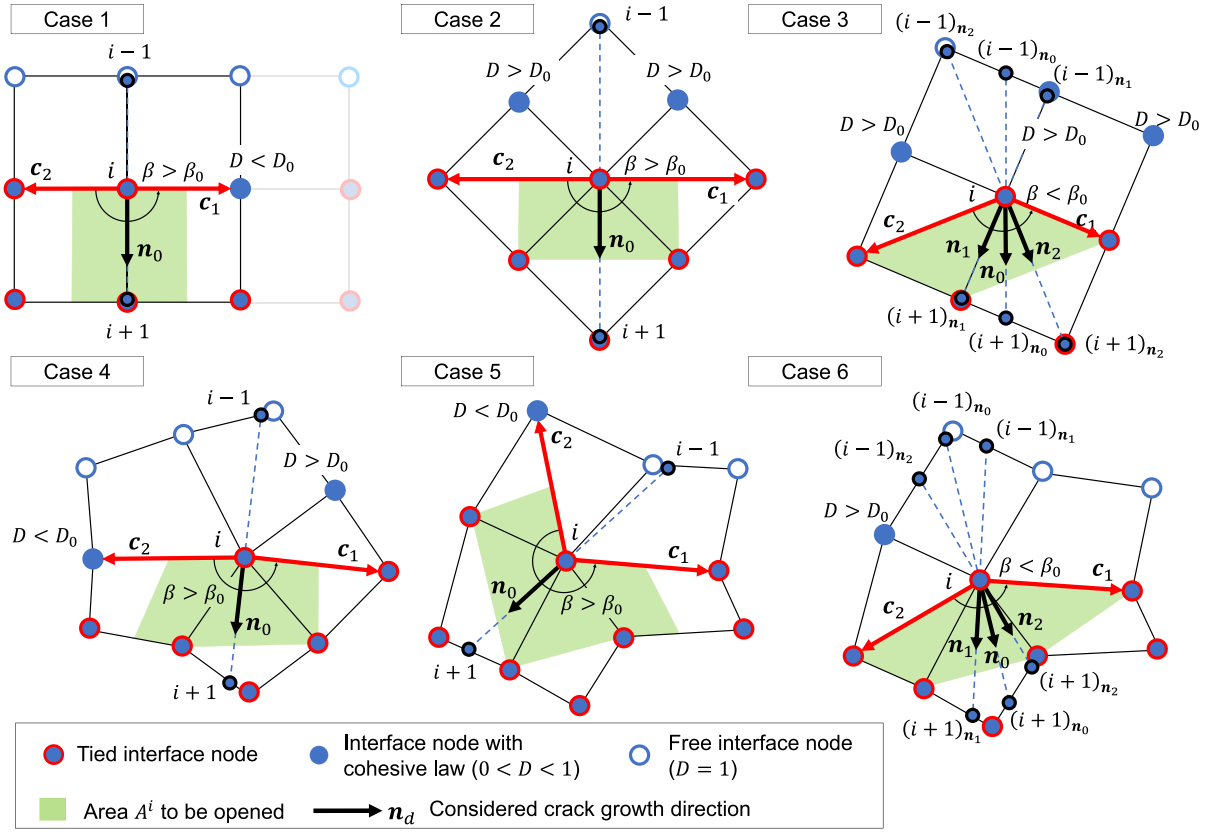

Fig. 7. Examples of crack front configurations around the node i following the general definition of the area. If $\beta < \beta_0$, 3 crack growth directions are considered: $\boldsymbol{n}_1$, $\boldsymbol{n}_2$ and $\boldsymbol{n}_0$. If $\beta > \beta_0$, the crack growth direction $\boldsymbol{n}_0$ is solely considered. The openings are retrieved at node $i-1$ at the intersection between the perimeter edges and the crack growth direction on the debonded side.

Finally, l^i, l^{i-1} and θ^0 are defined for the evaluation of the shape correction factor c_α^i. The characteristic length l^{i-1} is taken as the distance from i to $i-1$. Similarly to $i-1$, a point $i+1$ is defined on the bonded side and the length l^i is measured from i to $i+1$. It is recalled that the angles θ_U^0 and θ_L^0 define the crack tip opening angle through $\theta^0 = \theta_U^0 + \theta_L^0$, see Fig. 1. The angles θ_U^0 and θ_L^0 are taken as projected angles in the plane formed by the growth direction $\boldsymbol{n}_d$ and the normal to the interface.

In the definition of the area A^i, a series of particular cases have to be considered for a wider application of the method. These cases, listed in Fig. 8, occur when only 1 to 3 consecutive nodes are bonded on the perimeter. They can be found at corners of rectangular bonded areas or at geometrical free edges. Following the convex definition ($\beta < \beta_0$), the standard 3 crack growth directions are considered. Rather, the particularity lies in the definition of the area A^i. For some of these particular cases, the area is defined differently for each growth direction $\boldsymbol{n}_d$, thus designated $\left(A^i\right)_{\boldsymbol{n}_d}$. The definition of the area A^i for each situation is illustrated in Fig. 8. It should be noted that all these particular cases follow the general case for the remaining of the algorithm.

With all necessary quantities defined, the VCCT is applied for each of the considered crack growth directions. The releasing of the tied condition at node i is triggered when $ERR \geq G_c$ as explained in the previous subsections. When two possible growth directions are triggered at node i in the same time increment, the direction maximising the ratio $\frac{ERR}{G_c}$ is chosen as suggested in [42]. However, for the particular cases of Fig. 8, the direction $\boldsymbol{n}_0$ with an expected larger delaminated area is preferred over directions $\boldsymbol{n}_1$ and $\boldsymbol{n}_2$. It should be clarified that the impact of the triggering growth direction on the following crack propagation modelled by the cohesive law is limited to the energy to be dissipated $A^i G_c$.

Finally, it should be mentioned that the algorithm is fed with adjacent elemental history variables through a built-in user subroutine in LS-DYNA. The latter allows to sync non-local information between neighbouring elements distributed in different memory partitions (computational nodes). The shared information comprises the elemental contribution to the interface forces at node i, the current position of the nodes, the tied status and damage value at the nodes.

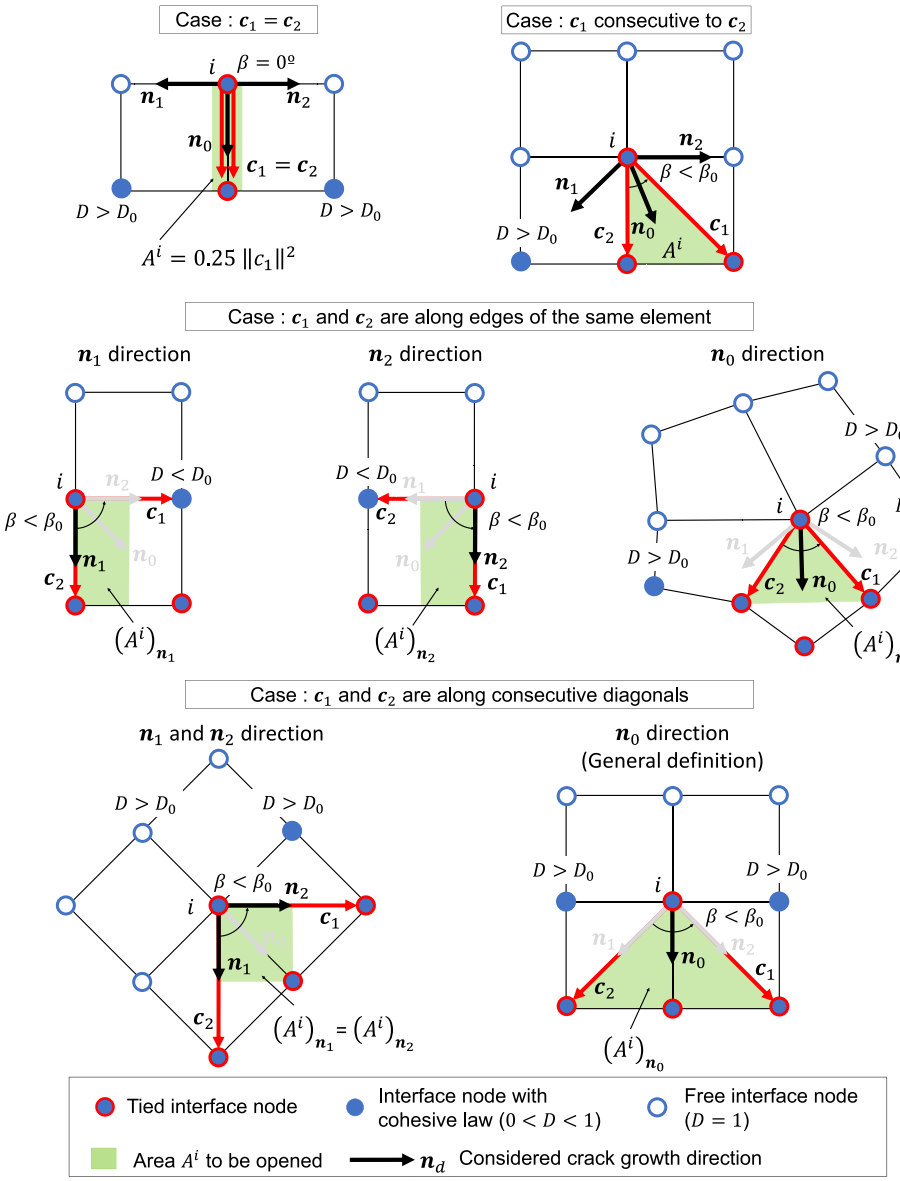

Fig. 8. Particular cases considered for the definition of the area A^i. These cases occur when only 1 to 3 consecutive nodes are bonded on the perimeter.

3. Validation

In this section, various numerical examples are presented to assess the ability of the adapted ERR-Cohesive method in modelling arbitrarily shaped delamination fronts with distorted large elements. Firstly, standard DCB and ENF tests are simulated with distorted elements and a mesh not aligned with the crack front. Then, the case of a plate with an initial rectangular crack transitioning towards a steady-state circular crack front is presented. Finally, the Reinforced-DCB test with an evolving shape of the delamination front is modelled and compared to the experimental results from Carreras et al. [38].

3.1. DCB and ENF

The DCB and ENF tests from a benchmark proposed by Krueger [43] are used to model a straight propagation in pure mode I and pure mode II. It is recalled that the constitutive model had been validated under mixed mode propagation in a previous publication [33]. The dimensions and material properties are extracted from the benchmark proposed by Krueger [43]. They are summarised respectively in Fig. 9 and Table 1. The laminate is made of unidirectional carbon-FRP layers, aligned along the

Table 1
Material and interface properties used in the different validation tests.

Property	DCB	ENF	Square plate	Reinforced-DCB	Units
Reference	[43]	[43]	[37]	[38]	
Substrate properties					
Material name	T300/1076	IM7/8552	Aluminium	Carbon-FRP	
E_{11}	139.4	161.0	70	154	GPa
$E_{22} = E_{33}$	10.16	11.38	–	8.5	GPa
$G_{12} = G_{13}$	4.6	5.2	–	4.2	GPa
G_{23}	3.54	3.9	–	3.036	GPa
$\nu_{12} = \nu_{13}$	0.30	0.32	0.3	0.35	–
ν_{23}	0.436	0.45	–	0.40	–
ρ	1500[a]	1500[a]	2700	1500[b]	kg m^{-3}
Interface properties					
G_{Ic}	0.170	0.212	0.212	0.305	kJ m^{-2}
G_{IIc}	0.494	0.774	0.774	2.77	kJ m^{-2}
η	1.62	2.1	2.1	2.05	–

[a] Not specified in [43], a standard value is used.
[b] Not specified in [38], a standard value is used.

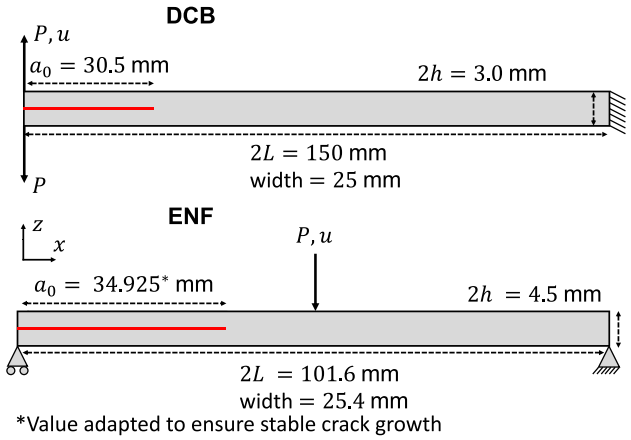

Fig. 9. Benchmark configurations used for the DCB and ENF tests [43].

longitudinal direction of the coupons. In order to ensure stable crack growth, the initial crack length has been adapted to $a_0 = 0.69L$ for the ENF case.

The presented ERR-Cohesive method is employed with three different meshes, visible in the results in Fig. 11 and Fig. 13. The first model is a regular 3 mm mesh used as reference. A regular 4.5 mm mesh oriented at 45° with respect to the crack direction is used to evaluate the method in a case where the mesh is not orthogonal with respect to the crack front. To allow for a quad-only 45° mesh, this latter is defined such that the specimen boundaries correspond to the outermost continuous element diagonals. The outermost interface node pair is set free to respect for the initially bonded area that is marked on the meshes shown in the result figures. Finally, the method is challenged with a distorted mesh presenting element lengths ranging from 1 to 5 mm. Apart from the element length limits, the distorted mesh meets typical quality criteria which can be found in the industry about skewness, taper and aspect ratio. These different mesh configurations are coarse in the sense that the elements are larger than the expected FPZ for such interface.

Some simulations parameters share common definition for all the models using the ERR-Cohesive method presented afterwards. That is, the load is introduced through an imposed displacement following the ramp-up phase of a sinusoidal shape with a termination time of 0.5 s. No global damping is applied to the models. However, as mentioned in Section 2.4, a local interface damping is used at the nodes where the cohesive law is acting. The cohesive stiffness is set such that the interface stable time step is 0.25 μs [33]. Finally, the two parameters of the algorithm for arbitrarily shaped crack are recalled: $D_0 = 0.25$ and $\beta_0 = 150°$.

The force–displacement curves obtained for the different meshes are compared to the analytical solution obtained from the Corrected Beam Theory (CBT) [44–46] in Fig. 10 and Fig. 12, respectively, for the DCB and ENF tests. In Fig. 11 and Fig. 13, some crack propagation states are presented, corresponding to different values of imposed displacement. The damage plot for the ERR-Cohesive method is shown together with the crack length obtained from the analytical solution. For the present method, it is worth recalling that the damage value at a given node can be related to the fraction of assigned area which has been opened, see Eq. (16). For example, if a node of a regular mesh has a damage value of 0.5, the crack front is expected to be halfway through the following element.

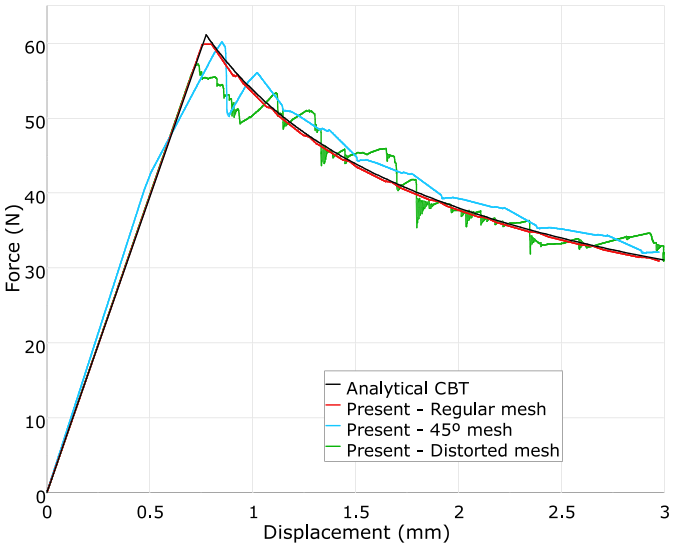

Fig. 10. DCB force–displacement results for 3 different meshes: a regular mesh, a distorted mesh and a regular mesh oriented at 45° with respect to the propagation direction. The different meshes are visible for 3 propagations states in Fig. 11.

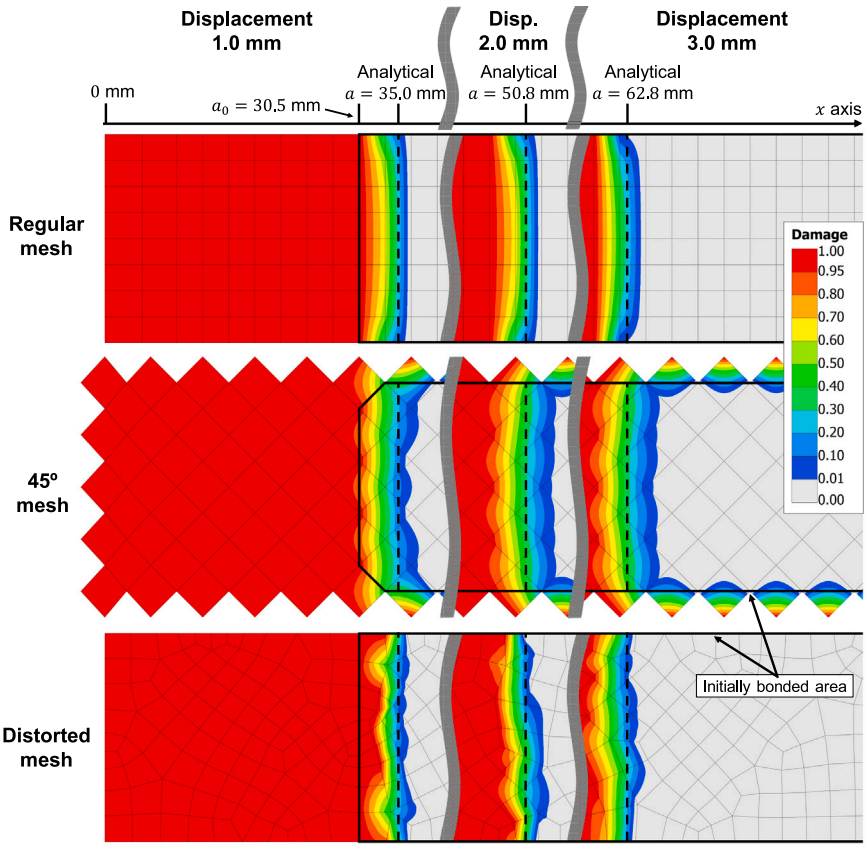

Fig. 11. DCB propagation states for the 3 different meshes. The 3 propagations states corresponding to displacements of 1 mm, 2 mm and 3 mm are superposed in the same mesh representation.

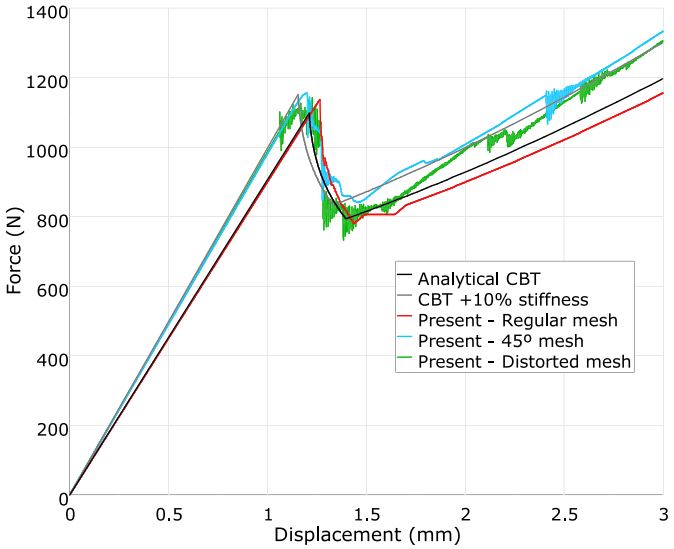

Fig. 12. ENF force–displacement results for 3 different meshes: a regular mesh, a distorted mesh and a regular mesh oriented at 45° with respect to the propagation direction. The different meshes are visible for 2 propagations states in Fig. 13.

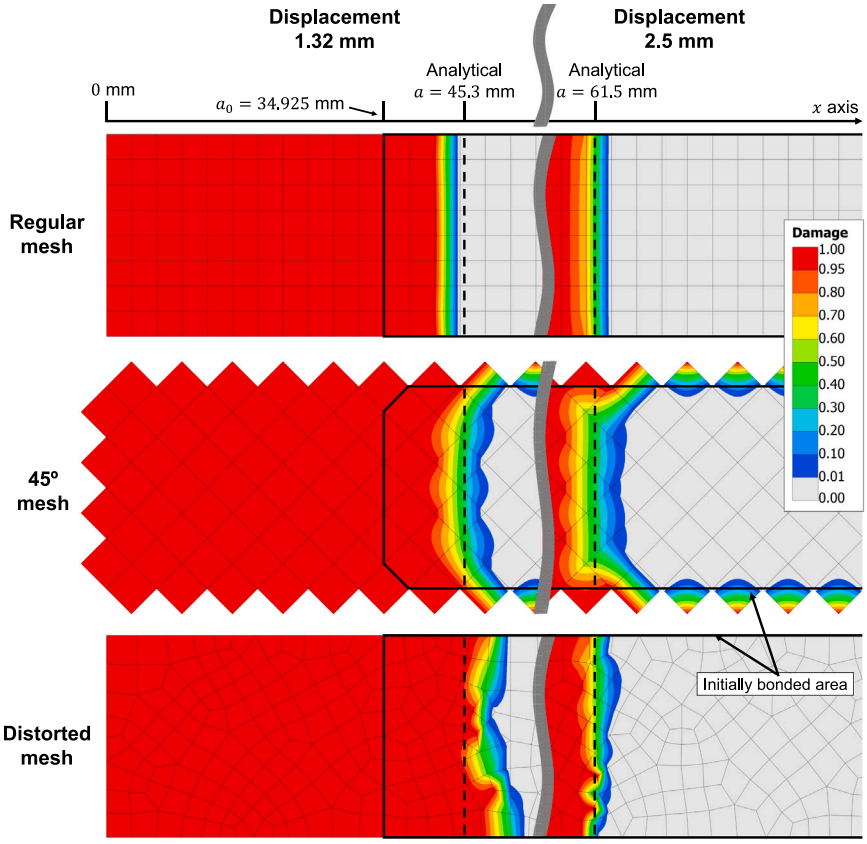

Fig. 13. ENF propagation states for the 3 different meshes. The propagations states corresponding to displacements of 1.32 mm and 2.5 mm are superposed in the same mesh representation.

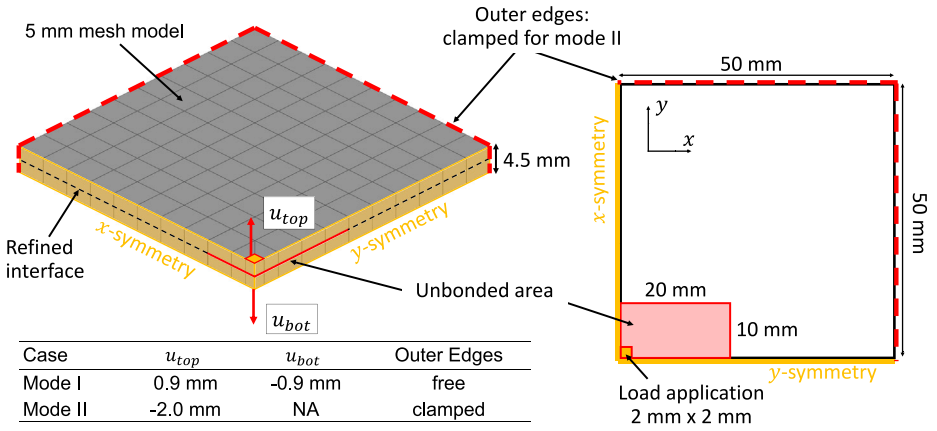

Case	u_{top}	u_{bot}	Outer Edges
Mode I	0.9 mm	-0.9 mm	free
Mode II	-2.0 mm	NA	clamped

Fig. 14. Geometry of the square plate with unbonded rectangular area [37]. Symmetry conditions are applied such that a quarter of the plate is represented. Two different cases are defined to load separately the interface in mode I and mode II.

As expected from [33], the results for the regular mesh are excellent as they closely follow the analytical solution both for the force–displacement curve and for the crack propagation. The results for the 45° mesh and the distorted mesh are considered good in view of the suboptimal mesh configurations employed. The difference with respect to the analytical solution is relatively low and the instabilities are limited.

Looking closely at the DCB force–displacement curve of the 45° mesh in Fig. 10, an early initial propagation can be observed at a force of about 42 N. This early propagation is due to ERR concentrations at the sharp corners delimiting the bonded area. This overestimation of the ERR has been observed by others authors [26,27]. However, in the present case, the energy dissipation mechanism ensures the force to reach the expected values. Then, the following nodes do not experience this unrealistic ERR concentration thanks to the damage mechanism still acting at the previous nodes, smoothing the crack tip forces along the front. It should be clarified that the reversed thumbnail shape of the crack front appearing at a displacement of 1 mm is caused by the front being merged with the initially unbonded outermost free node. The real shape of the crack front can be seen for a 2 mm or 3 mm imposed displacement. Thus, the presented VCCT evaluation algorithm allows to detect the correct growth direction, although the mesh is not aligned with the crack front.

The distorted mesh case further exemplifies the robustness of the method. The crack front remains relatively straight despite the mesh distortion. Additionally, the accuracy of the force–displacement curve shows that the algorithm globally dissipates the correct amount of energy. The energy dissipated by the cohesive law through Eq. (16) is highly dependent on the area to be opened A considered by the VCCT algorithm explained on Section 2.5. Therefore, the correct force–displacement curve and the low instabilities show the ability of the algorithm in evaluating the area to be opened in distorted meshes. Finally, it can be observed that the analytical crack front corresponds to damage values around 0.20 to 0.30 (cyan colour) in the present method. This is an indication for the chosen empirical value of $D_0 = 0.25$ in Section 2.5.

In the ENF test, some instabilities have been observed when applying the method with the solid-shell formulation employed, corresponding to LS-DYNA reduced integration thick shell ELFORM 5. Such instabilities are greatly reduced by rising the anti-hourglass coefficient. However, the latter artificially increases the stiffness of the element in the case of bending along the element diagonals. For this reason, the initial stiffness of the 45° mesh and the distorted mesh is higher than the expected one according to the analytical solution, see Fig. 12. For a better comparison, the analytical solution with a 10% stiffness increase is also plotted. At a displacement of 1.32 mm, the nearly-unstable crack growth phase ends with accurate propagation states observed for the regular and 45° mesh. The distorted mesh shows a slightly advanced crack growth compared to the analytical solution due to a short unstable growth episode. The following, more stable, propagation phase is well captured by all the meshes. These ENF results confirm the accuracy of the method in modelling mode II propagation in non-aligned and distorted coarse mesh.

3.2. Square plate

The following example is a square plate with an unbonded rectangular area in its centre. Proposed by De Carvalho et al. [37], it is used to evaluate the ability of the method in modelling a non-self-similar crack growth. The crack front transitions from the initial rectangular shape to a steady-state circular shape.

Referring to the model illustrated in Fig. 14, the aluminium plate is 4.5 mm thick with a side length of 100 mm. It is made from two 2.25 mm-thick plates bonded together, except for a central rectangular area. Only a quarter of the model is simulated by applying symmetry conditions. An imposed displacement is applied in a square area at the centre of the plate. Mode I is created by applying an upward displacement on the top side and a downward displacement on the lower side, while the plate is free of any boundary condition apart from the symmetry conditions. Mode II is created by clamping the outer edges and applying a downward displacement on the top side of the plate. The properties of the material and the bonding interface are shown in Table 1.

The present method is used with a 2 mm and a 5 mm mesh. As comparison, an Abaqus/Standard® CZM simulation with a 0.5 mm mesh is also performed. Apart from the fracture toughness in Table 1, the conventional cohesive elements use a penalty stiffness of $k_I = k_{II} = 5.0 \times 10^5$ MPa.mm^{-1} and a strength of $X_I = X_{II} = 30$ MPa.

Additionally, analytical solutions have been derived considering a circular crack front, see Appendix. In the present case, the crack front becomes circular once steady-state growth is reached with a radius of the delaminated area corresponding to the diagonal of the initial rectangle: $a = 22.36$ mm. After that, the front is perfectly circular for mode I due to the absence of boundary conditions on the outer edges. For mode II, the front is not perfectly circular due to the square shape of the clamped outer edges. Still, the front is assumed circular for moderately small crack radius. Instead of the 100 × 100 plate dimension, a substitute outer radius is considered for the analytical solution following $R = \sqrt{(100 \times 100/\pi)}$ [47].

For mode I, the force–displacement curves are presented in Fig. 15, and the crack propagation states for two displacements values are shown in Fig. 16. The results of the present method are considered close to the refined CZM model. At a displacement of 0.1 mm, the crack propagation has initiated on the longer side of the initially unbonded area. The present method correctly detects this initial propagation responsible for the stiffness change at a force around 250 N. This first propagation phase shows the ability of the method in modelling a non-self-similar growth. At a displacement of 0.25 mm, the crack front has recovered the steady-state circular propagation. The different models are well in agreement with the crack front radius of $a = 24.24$ mm predicted by the analytical solution. The excellent circular shape obtained under steady-state growth demonstrates that the propagation is independent to alignment of the mesh with respect to the crack front, refer to the 3 cases in Fig. 4.

The force–displacement curves for mode II are presented in Fig. 17, and the crack propagation states in Fig. 18. As previously explained, some instabilities occur in mode II when a low anti-hourglass coefficient is used. In this example, the anti-hourglass coefficient is kept low to limit the stiffness increase which would invalidate the comparison with CZM. Consequently, some instabilities can be observed, especially for the 2 mm elements presenting a high thickness-to-length ratio. These instabilities are visible through vibrations in the force–displacement curves and through a distinctive pattern where alternating damage values are obtained along parts of the crack front that are orthogonal to the mesh. Such instabilities under mode II propagation have also been observed by Brambilla et al. [25].

In addition, the CZM model presents a large FPZ length, estimated to 10.4 mm according to the expression by Soto et al. [48]. This large FPZ complicates the propagation state comparison between CZM and the present method. A non-linear damage colour scale is used for the CZM propagation shown in Fig. 18 as conventional cohesive elements present a highly non-linear relation between damage values and dissipated energy [49,50]. Arguably, the analytical crack state serves as a better reference. Nonetheless, the results are satisfactory as the force–displacement curves of the present method are close to the one obtained with CZM, especially the 5 mm mesh.

3.3. Reinforced-DCB

The Reinforced-DCB test is based on the experimental benchmark proposed by Carreras et al. [38]. The test is designed such that the shape of the crack front evolves notably from a concave to a convex shape. The experimental data [51] includes the measured shape of the delamination front at different propagation states. It is especially suitable to validate algorithm aiming to model arbitrarily shaped crack front.

The geometry of the sample is described in Fig. 19. For the numerical modelling, the nominal dimensions of the coupon are considered according to [52]. The load application is similar to a standard DCB test. Both the laminate of the main plate and the reinforcement are made of unidirectional Carbon-FRP plies oriented longitudinally, the properties of the ply and interface are presented in Table 1. The initial crack length is 35 mm. For more details on the experimental test, refer to [38].

The experiment has been modelled with the present method for a 1.8 mm and a 5.0 mm mesh. A CZM model with a 0.25 mm mesh made with Abaqus/Standard® is used for additional numerical comparison. The conventional cohesive elements use a penalty stiffness of $k_I = k_{II} = 1.0 \times 10^5$ MPa mm^{-1} and a strength of $X_I = X_{II} = 20$ MPa. This strength value has been reduced compared to the original strength [52] to avoid mesh size dependency [3].

The force–displacement results are shown in Fig. 20. The curves of the specimen A, B and C show the cyclic loading which have been used to measure the shape of the crack front at different propagation states, see [38]. The specimen D has been loaded without interruption. The different propagation states obtained numerically are compared to the experimental ones in Fig. 21. The results show that the present method is able to model the propagation both with the 1.8 mm and the 5 mm mesh. The force–displacement curves and the shape of the delamination front at the different propagation states are close to the experimental data.

Each propagation phase can be analysed more specifically. At a displacement of 6 mm, the first propagation phase is ending as the crack approaches the reinforcement. The delamination front is starting to be concave. The CZM crack appears slightly ahead of the experiment. After 6 mm, the force increases as the propagation reaches the reinforcement. At a displacement of 10 mm, this ascending phase is ending and an accurate concave crack front is clearly visible in all the models.

Before reaching the last propagation phase, a force peak can be seen at around 11 mm to 12.5 mm of applied displacement in the numerical models. The peak is followed by an unstable growth corresponding to the sudden reversal of the front concavity. The force peak is not present in the experiment. The fine-mesh CZM simulation shows that this force peak is not related to the ERR-Cohesive method. It is believed that this force peak is caused by an insufficient mesh resolution at the reinforcement borders due to the expected stress concentration at this point. A clear tendency can been seen in the results where the peak is being reduced with finer models. However, additional experimental factors cannot be discarded, such as unnoticeable plasticity at the bonded

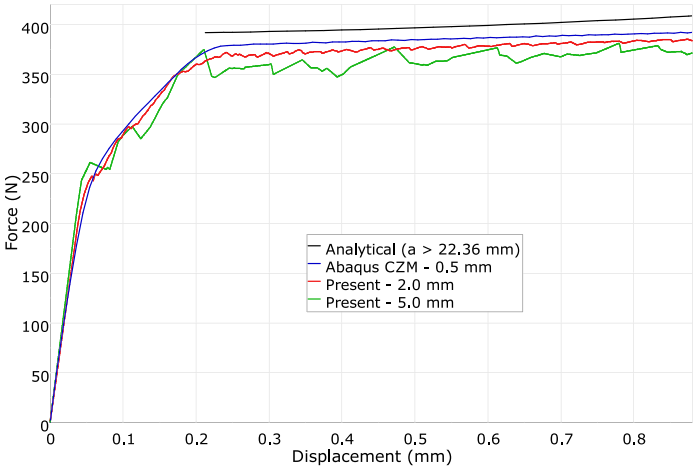

Fig. 15. Mode I force–displacement results for the square plate. The analytical solution is known once the steady-state circular crack front is recovered. See Fig. 16 for the propagation comparison.

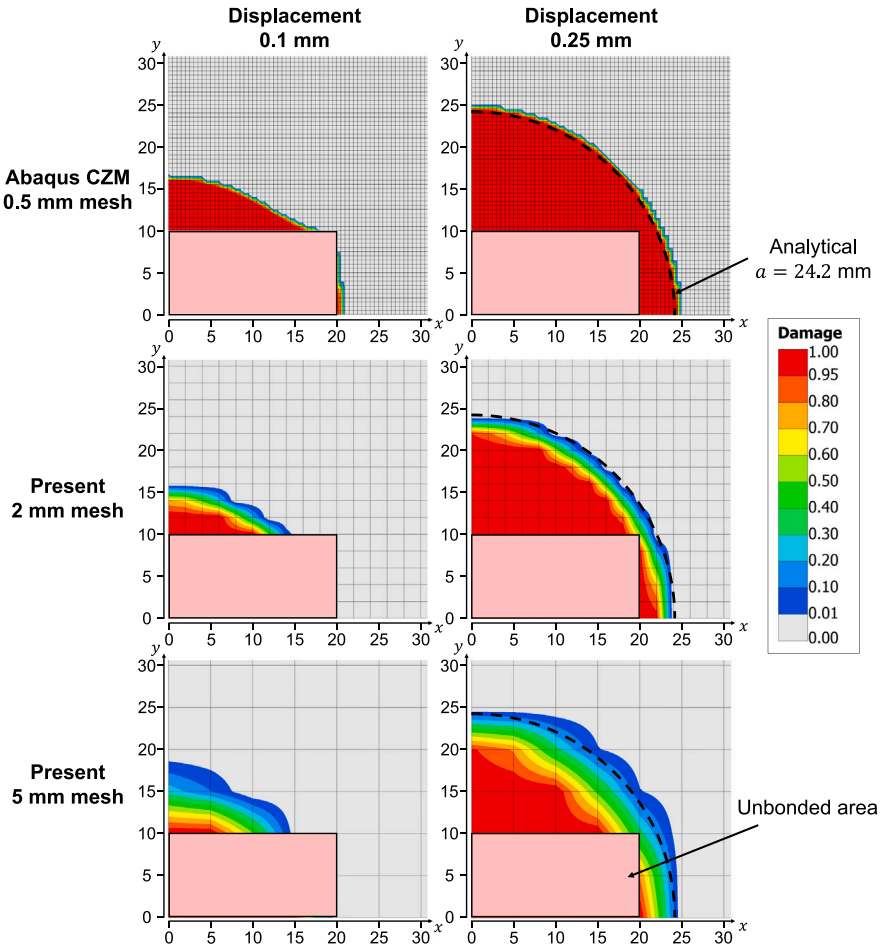

Fig. 16. Comparison of the mode I square plate results at two different states of propagation.

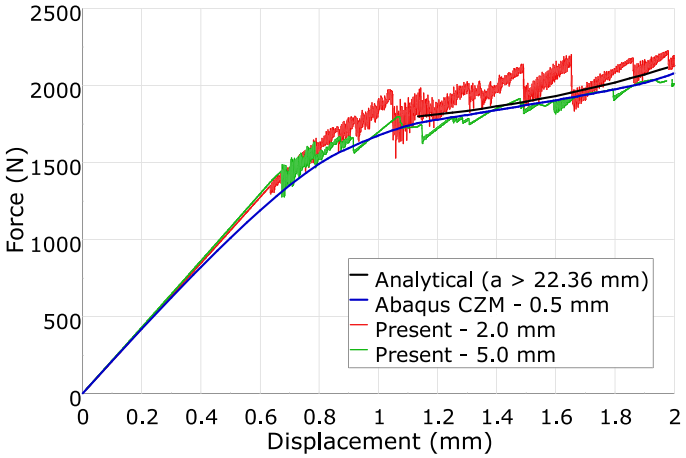

Fig. 17. Mode II force–displacement results for the square plate.

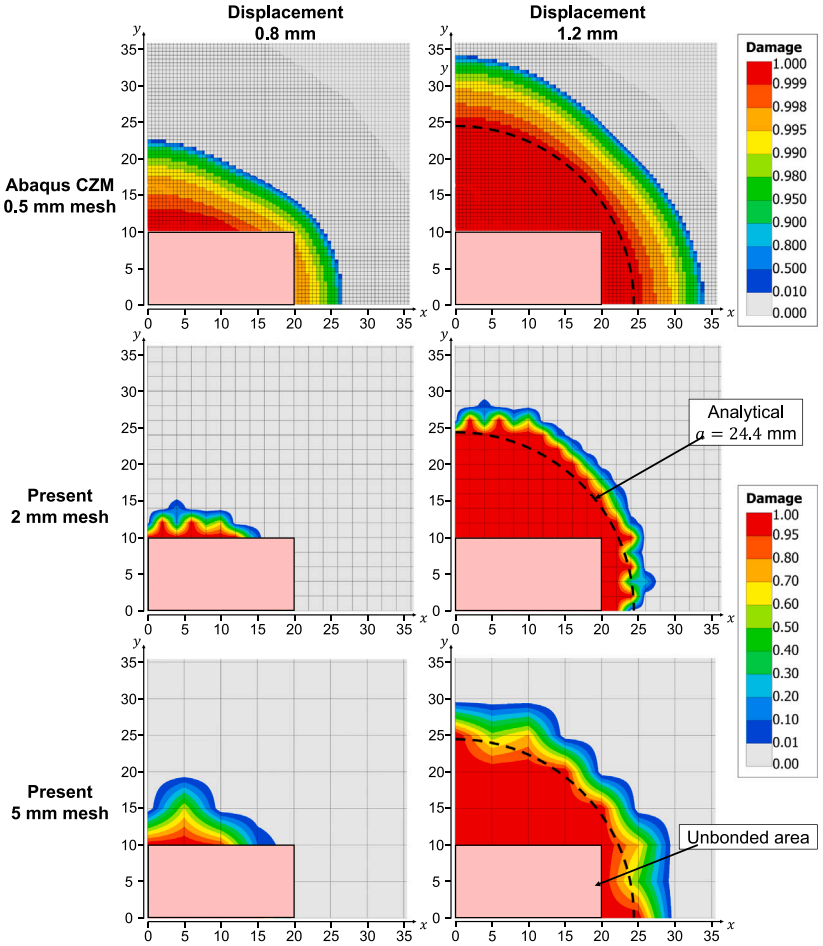

Fig. 18. Comparison of the mode II square plate results at two different states of propagation. The CZM results show a large FPZ. Thus, a non-linear damage colour scale is used to better estimate the position of the crack front. Instabilities are observed for the present method when high thickness-to-length ratio elements are used with a low anti-hourglass coefficient. These instabilities appear through alternating damage values along parts of the crack front that are orthogonal to the mesh.

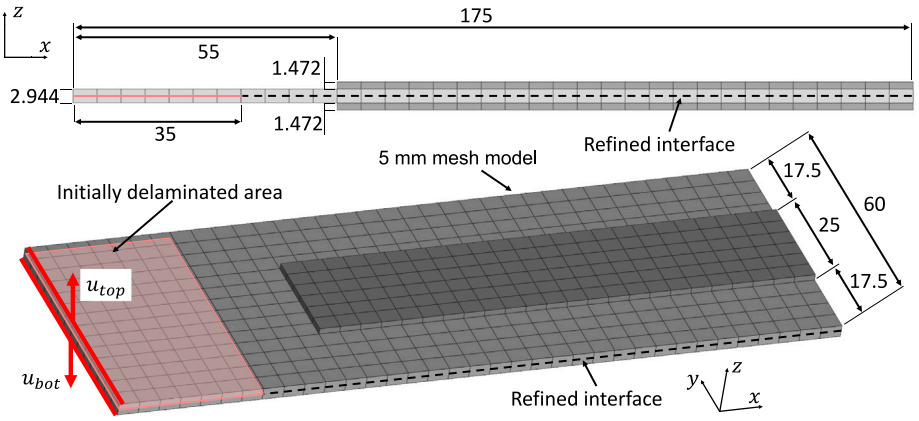

Fig. 19. Geometry of the Reinforced-DCB test according to [52].

interface between the reinforcement and the main plate, or the effect of some fibre bridging observed at the end of the experiment by Carreras et al.

Afterwards, the last propagation phase is reached as the crack front is beyond the reinforcement border. The delamination shape is now convex. At a 12 mm displacement, the numerical models capture well the front shape, but the crack is slightly ahead compared to the experiment. In the case of the 5 mm mesh, the corresponding plot in Fig. 21 is shown for a displacement of 12.5 mm, just after the unstable growth. The latter is delayed due to the high curvature of the crack front being poorly discretised by the coarse mesh.

Finally, at the end of the experiment, the propagation continues in a seemingly steady-state growth. The front shape is well captured apart from the outpaced growth. This final difference between the numerical and experimental results is believed to come from the mentioned fibre bridging, which appears at the main interface below the reinforcement. Overall, the results of present method are excellent considering that the large mesh employed is able to match the fine-mesh CZM results.

3.4. Discussion

The results show that the method is able to model the presented propagation tests with non-self-similar crack growth. This non-self-similarity is either caused by the mesh distortion or by the evolution of the front shape. Thus, the results indicate that the method does not inherit the self-similarity limitations of the VCCT.

The self-similarity hypothesis is important in the evaluation of the opening behind the crack front Δ_α^{i-1}. Traditionally, this opening is viewed as an estimation of the opening that would appear at node pair i due to a virtual self-similar crack growth. This virtual crack growth is used to evaluate the rate in the loss of elastic energy at the current propagation state. Similarly, the opposite idea could be argued where F_α^i can be seen as an estimation of the force necessary to close the opening Δ_α^{i-1}, representing a virtual closure of the current crack wake. With this latter consideration, it is intuitive that the propagation following the triggering of the growth criterion does not need to occur under self-similarity.

When the growth criterion is triggered (i.e. $G_T > G_c$), the front is allowed to propagate up to the next segment defined by the mesh (new line of nodes) by dissipating the corresponding amount of fracture energy AG_c. Thus, the dynamic of the propagation is solved through the cohesive law based on the stiffness response of the structure. Once the next segment is reached, the local crack front configuration is re-evaluated based on the new shape of the crack front, following the presented algorithm. The cohesive law, acting on the nodes in the vicinity, avoids the ERR concentrations traditionally appearing when the crack front is poorly discretised by the mesh.

For these reasons, the present method allows to relax the self-similarity hypothesis in terms of evolving crack front shape and mesh distortion provided that the mesh size is reasonable compared to the curvature of the front. The self-similarity in terms of varying mode-mixity has not been challenged in the presented propagation tests. However, it should be mentioned that the cohesive law has been designed to allow for changes in mode-mixity. Namely, the predefined energy AG_c is ensured to be accurately dissipated for any monotonic opening, including non-linear softening induced by a variation in mode-mixity. The fracture energy AG_c is updated for the current mode-mixity at each segment newly encountered. Thus, it is believed that the present method could account for evolving mode-mixity occurring at a reasonable rate compared to the element size.

Finally, the developed algorithm has two input parameters, D_0 and β_0. These parameters are not expected to be adjusted for specific propagation test and element size. It is recalled that the presented results have been obtained with fixed values, $D_0 = 0.25$ and $\beta_0 = 150°$, for all the presented propagation tests and employed meshes. Based on the authors' experience during the method development, the results are not very sensitive to the respective variations of β_0 in the $[140°, 160°]$ interval and D_0 in the $[0.20, 0.27]$ interval. Due to its geometrical nature, β_0 is not expected to need adjustment when using other modelling configurations. However, the damage threshold D_0 is related to the opening in the crack wake through the cohesive law. Thus, significant variations in the

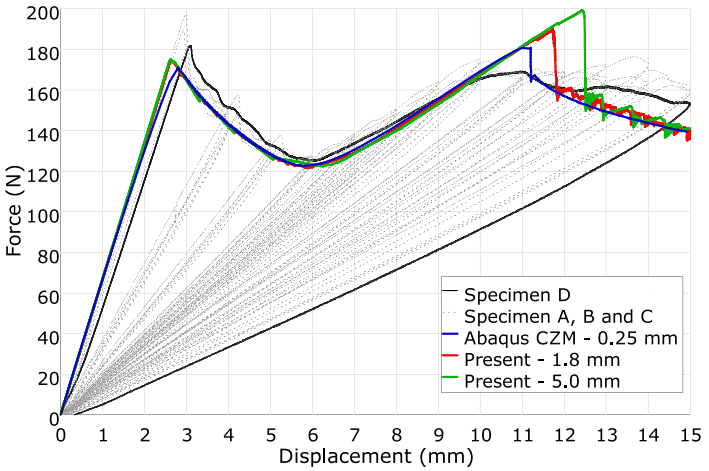

Fig. 20. Reinforced-DCB force–displacement results. The experimental results are taken from [51].

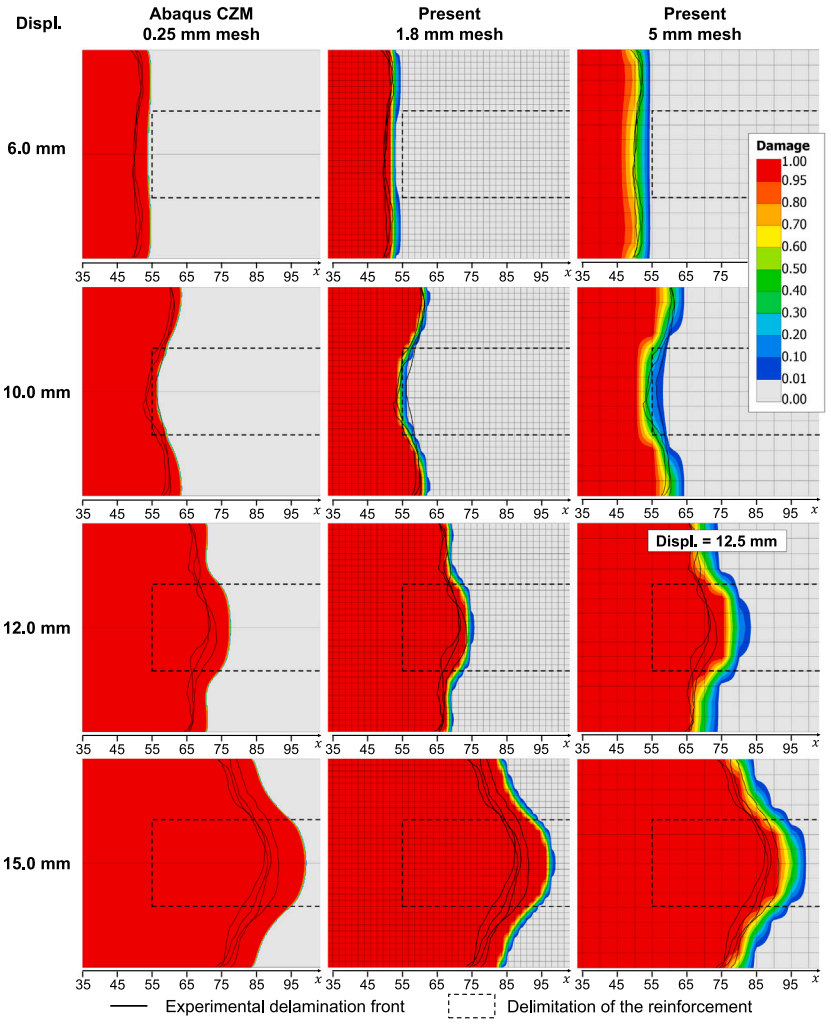

Fig. 21. Reinforced-DCB delamination front comparison. The experimental results are taken from [51].

cohesive law, element formulation and mesh size could affect the recommended $[0.20, 0.27]$ interval. In this case, it is advised to redefine this interval following the iterative process explained in Section 2.5 and summarised in Fig. 4.

4. Conclusions and outlook

4.1. Conclusions

In this article, a method has been presented for the modelling of arbitrarily shaped delamination fronts in composite materials. The crack propagation is predicted by an estimation of the ERR by means of the VCCT. An algorithm has been developed to apply the VCCT in cases where the crack front is not aligned with the mesh. Furthermore, the algorithm is designed to apply to large and distorted elements.

The presented algorithm is compatible with the energy dissipation mechanism of the previously published ERR-Cohesive method [33]. That is, a cohesive law is triggered when the VCCT-calculated ERR reaches the interface fracture toughness G_c. The cohesive damaging process ensures the correct amount of energy to be dissipated, given the mode-mixity that prevails.

The cohesive energy dissipation mechanism is essential for the accuracy of the ERR evaluation. With the traditional VCCT, a faster delamination growth is observed when the mesh is not aligned with the crack front. For this case, the crack growth rate is exaggerated by the overestimation of the ERR at sharp corners of the discretised front [25,26,28]. In the present method, the progressive damage mechanism acting at nodes in the vicinity of the crack front removes the binary nature of the VCCT (where nodes are either closed or opened). This allows for smoother crack tip forces along the front.

Several numerical examples have been carried out to illustrate the method. The DCB and ENF tests demonstrate the accuracy of the method when using distorted elements as well as meshes not aligned with the crack front. The example of a plate with planar propagation is used to show the ability of the method in modelling non-self-similar growth. Finally, the Reinforced-DCB test validates that the presented method can model an evolving crack front as observed experimentally.

The presented method is able to obtain results similar to conventional Cohesive Zone Modelling, but with large element ranging from 2 to 5 mm. Therefore, the extended ERR-Cohesive method emerges as an efficient solution for the modelling of crack propagation with engineering mesh. It opens possibilities for industrial applications where delamination propagation needs to be modelled in large structures.

4.2. Outlook

Classical materials are typically modelled in the transportation industry with a single through-the-thickness 5 mm shell. The conventional modelling of delamination in composite materials results in two additional refinements: out-of-plane and in-plane. The out-of-plane refinement is associated to the need of representing each ply interface prone to delamination. The in-plane refinement arises from the use of cohesive elements, which need to be smaller than the Fracture Process Zone of the interface, typically smaller than 1 mm.

The presented work is part of a wider strategy to enable the efficient modelling of delamination for large structure applications. To relieve the computational cost associated to the out-of-plane refinement, an adaptive modelling strategy is used [34,35]. Namely, the model starts in an unrefined state with a single through-the-thickness element. Interfaces are refined only when and where necessary. A method has been developed to recover the out-of-plane stress profile of laminated represented by a single through-the-thickness linear shell element [39]. The recovered stresses can be used to compute a refinement criterion at the different interfaces. The in-plane refinement is relieved by the use of the ERR-Cohesive method [33] extended to arbitrarily shaped front in the present work.

Naturally, the ERR-Cohesive method inherits some of the traditional limitations of the VCCT. Namely, mesh dependency might be observed when estimating the mixed-mode ERR at interfaces between plates of dissimilar compliance [11]. This is the case of interfaces between layers of different orientations or unsymmetrical cracks [53]. However, this effect is expected to be limited to fine modelling [11] and should not be critical for the present configuration where large elements are employed.

More importantly, the estimation of the ERR by the VCCT relies on the existence of an initial crack. Thus, the opening of initial cracks is the remaining aspect to be solved to ensure the transition between interface refinement and crack propagation. Then, it would constitute a complete delamination modelling strategy for large structures.

CRediT authorship contribution statement

Pierre M. Daniel: Writing – review & editing, Writing – original draft, Visualization, Validation, Software, Investigation, Conceptualization. **Johannes Främby:** Writing – review & editing, Validation, Software. **Martin Fagerström:** Writing – review & editing, Validation, Supervision. **Pere Maimí:** Writing – review & editing, Validation, Supervision, Funding acquisition.

Declaration of competing interest

The authors declare that they have no known competing financial interests or personal relationships that could have appeared to influence the work reported in this paper.

Data availability

No data was used for the research described in the article.

Acknowledgements

An important part of P.M. Daniel's work has been funded by Barcelona Technical Center S.L. (Btech[c]). The financial support of the Agencia de Suport a l'Empresa Catalana (ACCIÓ) through the grant ACE034/21/000015 is acknowledged. This work has also been partially funded by the Spanish Government (Ministerio de Ciencia e Innovación) under contract PID2021-126989OB-I00. M. Fagerström and J. Främby gratefully acknowledge the financial support through Vinnova's strategic innovation programme LIGHTer (LIGHTer Academy grant no. 2020-04526). Open Access funding provided thanks to the CRUE-CSIC agreement with Elsevier.

Appendix. Circular plate with central delamination (Analytical solution)

The analytical model consider an quasi-isotropic circular plate with a central delamination of radius a illustrated in Fig. A.22. In the following, the derivations for mode II and mode I are presented.

A.1. Mode II

The derivations for mode II are based on the work by Wagih et al. [47]. The force–displacement relationship is expressed as

$$F = \frac{1}{C_b^{II} + C_s^{II}} u + \frac{1}{C_m^{II}} u^3, \tag{A.1}$$

where C_b^{II}, C_s^{II} and C_m^{II} are respectively the bending, shear and membrane compliance. They are defined as

$$C_b^{II} = \frac{R^2 + 3a^2}{16\pi D}, \tag{A.2a}$$

$$C_s^{II} = \frac{1}{k_s h}, \tag{A.2b}$$

$$C_m^{II} = \frac{R^2}{k_m^{II} h}, \tag{A.2c}$$

where the bending stiffness D reads

$$D = \frac{E_{11} h^3}{12\left(1 - \nu_{12}\nu_{21}\right)}, \tag{A.3}$$

and the stiffness parameters k_s and k_m are expressed as [54]

$$k_s = \frac{4\pi G_{13}}{3} \frac{E_{11}}{E_{11} - 4\upsilon_{13} G_{13}} \left(\frac{4}{3} + \ln\left(\frac{R}{r_c}\right)\right)^{-1}, \tag{A.4a}$$

$$k_m^{II} = \frac{\pi E_{11}}{1 - \nu_{12}} \frac{353 - 191\nu_{12}}{648}, \tag{A.4b}$$

with r_c being the contact radius between the impactor and the plate.

The crack growth is defined by the propagation criterion from LEFM:

$$\mathrm{ERR} = -\frac{\partial U}{\partial A} = G_c. \tag{A.5}$$

The elastic energy U is expressed by integrating Eq. (A.1) as

$$U = \int F du = \frac{1}{2\left(C_b^{II} + C_s^{II}\right)} u^2 + \frac{1}{4C_m^{II}} u^4, \tag{A.6}$$

and defining $\partial A = 2\pi a \partial a$ for a circular crack. Injecting into Eq. (A.5), it is obtained

$$G_c = \frac{1}{2} \frac{\partial C_b^{II}}{\partial a} \frac{1}{\left(C_b^{II} + C_s^{II}\right)^2} \frac{1}{2\pi a} u^2, \tag{A.7}$$

from which the crack radius can be expressed as a function of the displacement by

$$a = \sqrt{\frac{1}{3}\left(16\pi D\left(\frac{u}{F_{dn}} - C_s^{II}\right) - R^2\right)}, \tag{A.8}$$

with

$$F_{dn} = \sqrt{\frac{32}{3}\pi^2 G_c D}. \tag{A.9}$$

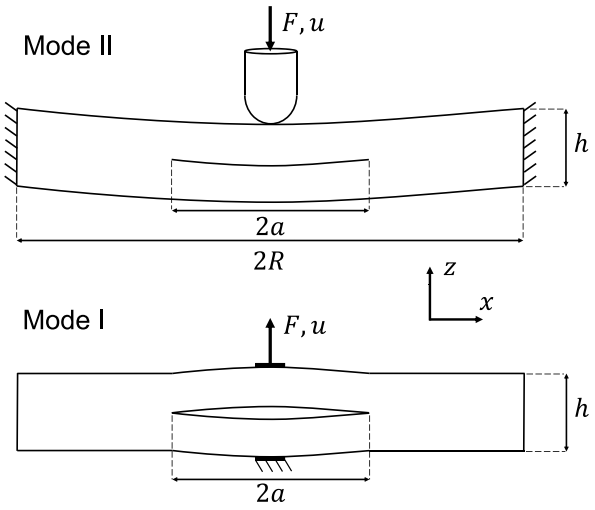

Fig. A.22. Representation of the circular plate with central delamination for mode I and mode II loading.

The force–displacement curve under propagation is obtained by updating the bending compliance C_b^{II} in Eq. (A.1) with the corresponding crack length radius a based on Eq. (A.8).

A.2. Mode I

The mode I solution is derived similarly with the additional hypothesis that the shear compliance is negligible. The force is defined as

$$F = \frac{1}{C_b^I}u + \frac{1}{C_m^I}u^3, \tag{A.10}$$

where the compliances are adapted to

$$C_b^I = \frac{a^2}{\pi D}, \tag{A.11a}$$

$$C_m^I = 8\frac{a^2}{k_m^I h}, \tag{A.11b}$$

with the stiffness parameter [54]:

$$k_m^I = \frac{191\pi E_{11}}{648}. \tag{A.12}$$

The elastic energy expressed as

$$U = \int F du = \frac{1}{2C_b^I}u^2 + \frac{1}{4C_m^I}u^4 \tag{A.13}$$

is injected in Eq. (A.5) and the crack radius is expressed as

$$a = \sqrt[4]{\frac{1}{2\pi G_c}\left(\pi D u^2 + \frac{1}{16}k_m^I h u^4\right)}. \tag{A.14}$$

The force–displacement curve under propagation is obtained by updating the compliances in Eq. (A.10) with the corresponding crack length radius a based on Eq. (A.14).

References

[1] Davila CG, Camanho P, de Moura M. Mixed-mode decohesion elements for analyses of progressive delamination. In: 19th AIAA applied aerodynamics conference. Reston, Virigina: American Institute of Aeronautics and Astronautics; 2001.
[2] Turon A, Camanho P, Costa J, Dávila C. A damage model for the simulation of delamination in advanced composites under variable-mode loading. Mech Mater 2006;38:1072–89.
[3] Turon A, Dávila C, Camanho P, Costa J. An engineering solution for mesh size effects in the simulation of delamination using cohesive zone models. Eng Fract Mech 2007;74:1665–82.
[4] Bak BLV, Lindgaard E, Lund E. Analysis of the integration of cohesive elements in regard to utilization of coarse mesh in laminated composite materials. Internat J Numer Methods Engrg 2014;99:566–86.

[5] Russo R, Chen B. Overcoming the cohesive zone limit in composites delamination: modeling with slender structural elements and higher-order adaptive integration. Internat J Numer Methods Engrg 2020;121:5511–45.
[6] Selvaraj J, Mukhopadhyay S, Kawashita LF, Hallett SR. Modelling delaminations using adaptive cohesive segments with rotations in dynamic explicit analysis. Eng Fract Mech 2021;245:107571.
[7] Rice JR. A path independent integral and the approximate analysis of strain concentration by notches and cracks. J Appl Mech 1968;35:379–86.
[8] Ishikawa H, Kitagawa H, Okamura H. J-integral of a mixed mode crack and its application. In: Mechanical behaviour of materials. Vol. 3, (August):Elsevier; 1980, p. 447–55.
[9] Judt PO, Ricoeur A. Crack growth simulation of multiple cracks systems applying remote contour interaction integrals. Theor Appl Fract Mech 2015;75:78–88.
[10] Rybicki E, Kanninen M. A finite element calculation of stress intensity factors by a modified crack closure integral. Eng Fract Mech 1977;9:931–8.
[11] Krueger R. Virtual crack closure technique: History, approach, and applications. Appl Mech Rev 2004;57:109–43.
[12] Carreras L, Lindgaard E, Renart J, Bak B, Turon A. An evaluation of mode-decomposed energy release rates for arbitrarily shaped delamination fronts using cohesive elements. Comput Methods Appl Mech Engrg 2019;347:218–37.
[13] McElroy M. An enriched shell finite element for progressive damage simulation in composite laminates. NASA/TP–2016-219211, 2016.
[14] Orifici AC, Thomson RS, Degenhardt R, Bisagni C, Bayandor J. Development of a finite-element analysis methodology for the propagation of delaminations in composite structures. Mech Compos Mater 2007;43:9–28.
[15] Zou Z, Reid S, Li S, Soden P. Application of a delamination model to laminated composite structures. Compos Struct 2002;56:375–89.
[16] Smith SA, Raju IS. Evaluation of stress-intensity factors using general finite-element models. vol. 29, ASTM STP 1332; 1999,
[17] Okada H, Higashi M, Kikuchi M, Fukui Y, Kumazawa N. Three dimensional virtual crack closure-integral method (VCCM) with skewed and non-symmetric mesh arrangement at the crack front. Eng Fract Mech 2005;72:1717–37.
[18] Xie D, Biggers SB. Strain energy release rate calculation for a moving delamination front of arbitrary shape based on the virtual crack closure technique. Part I: Formulation and validation. Eng Fract Mech 2006;73:771–85.
[19] Xie D, Biggers SB. Strain energy release rate calculation for a moving delamination front of arbitrary shape based on the virtual crack closure technique. Part II: Sensitivity study on modeling details. Eng Fract Mech 2006;73:786–801.
[20] Pietropaoli E, Riccio A. On the robustness of finite element procedures based on Virtual Crack Closure Technique and fail release approach for delamination growth phenomena. Definition and assessment of a novel methodology. Compos Sci Technol 2010;70:1288–300.
[21] Wu H, Settgast RR, Fu P, Morris JP. An enhanced virtual crack closure technique for stress intensity factor calculation along arbitrary crack fronts and the application in hydraulic fracturing simulation. Rock Mech Rock Eng 2021;54:2943–57.
[22] Liu YP, Chen CY, Li GQ. A modified zigzag approach to approximate moving crack front with arbitrary shape. Eng Fract Mech 2011;78:234–51.
[23] Liu YP, Li GQ, Chen CY. Crack growth simulation for arbitrarily shaped cracks based on the virtual crack closure technique. Int J Fract 2014;185:1–15.
[24] Marjanović M, Meschke G, Vuksanović D. A finite element model for propagating delamination in laminated composite plates based on the Virtual Crack Closure method. Compos Struct 2016;150:8–19.
[25] Brambilla P, Bisagni C, Dávila CG. Modeling of delamination in composite structures under static and fatigue loading. (Master thesis), Politecnico Di Milano; 2012.
[26] Martulli LM, Bernasconi A. An efficient and versatile use of the VCCT for composites delamination growth under fatigue loadings in 3D numerical analysis: the Sequential Static Fatigue algorithm. Int J Fatigue 2023;170.
[27] McElroy MW. An enriched shell finite element for progressive damage simulation in composite laminates. (Doctoral thesis), Raleigh: North Carolina State University; 2016.
[28] De Carvalho NV, Ramnath M, Mabson GE, Krueger R. An explicit delamination propagation algorithm to simulate delamination growth under quasi-static and fatigue loading without re-meshing using virtual crack closure technique and progressive nodal release. J Compos Mater 2022;56:2063–81.
[29] Mabson GE, De Carvalho NV, Krueger R. VCCT with progressive nodal release for simulating mixed-mode delamination: Formulation, algorithmic improvements and implications. In: American society for composites 2018. Lancaster, PA: DEStech Publications, Inc.; 2018.
[30] Mabson G, Deobald L, Dopker B. Fracture interface elements for the implementation of the virtual crack closure technique. In: 48th AIAA/ASME/ASCE/AHS/ASC structures, structural dynamics, and materials conference. Reston, Virigina: American Institute of Aeronautics and Astronautics; 2007, p. 1–11.
[31] De Carvalho NV, Krueger R, Mabson GE, Deobald LR. Combining progressive nodal release with the virtual crack closure technique to model fatigue delamination growth without re-meshing. In: 2018 AIAA/ASCE/AHS/ASC structures, structural dynamics, and materials conference. Reston, Virginia: American Institute of Aeronautics and Astronautics; 2018.
[32] De Carvalho N, Mabson G, Krueger R, Deobald L. A new approach to model delamination growth in fatigue using the virtual crack closure technique without re-meshing. Eng Fract Mech 2019;222:106614.
[33] Daniel PM, Främby J, Fagerström M, Maimí P. An efficient ERR-Cohesive method for the modelling of delamination propagation with large elements. Composites A 2023;167:107423.
[34] Främby J, Fagerström M, Karlsson J. An adaptive shell element for explicit dynamic analysis of failure in laminated composites Part 1: Adaptive kinematics and numerical implementation. Eng Fract Mech 2020;240:107288.
[35] Främby J, Fagerström M. An adaptive shell element for explicit dynamic analysis of failure in laminated composites Part 2: Progressive failure and model validation. Eng Fract Mech 2021;244:107364.
[36] LSTC and ANSYS Inc. LS-DYNA R11.1.0. 2019.
[37] De Carvalho NV, Ratcliffe JG. A cohesive element formulation for simulation of general mode I, II and III delamination. NASA/TM-20220002081, 2022.
[38] Carreras L, Renart J, Turon A, Costa J, Bak BLV, Lindgaard E, et al. A benchmark test for validating 3D simulation methods for delamination growth under quasi-static and fatigue loading. Compos Struct 2019;210:932–41.
[39] Daniel PM, Främby J, Fagerström M, Maimí P. Complete transverse stress recovery model for linear shell elements in arbitrarily curved laminates. Compos Struct 2020;252:112675.
[40] Irwin GR. Fracture. Vol. 970, 1958, p. 551–90.
[41] Benzeggagh M, Kenane M. Measurement of mixed-mode delamination fracture toughness of unidirectional glass/epoxy composites with mixed-mode bending apparatus. Compos Sci Technol 1996;56:439–49.
[42] Carreras L, Bak B, Turon A, Renart J, Lindgaard E. Point-wise evaluation of the growth driving direction for arbitrarily shaped delamination fronts using cohesive elements. Eur J Mech A Solids 2018;72:464–82.
[43] Krueger R. A summary of benchmark examples to assess the performance of quasi-static delamination propagation prediction capabilities in finite element codes. J Compos Mater 2015;49:3297–316.
[44] Reeder JR, Demarco K, Whitley KS. The use of doubler reinforcement in delamination toughness testing. Composites A 2004;35:1337–44.
[45] Allix O, Ladevéze P, Corigliano A. Damage analysis of interlaminar fracture specimens. Compos Struct 1995;31:61–74.
[46] Mi Y, Crisfield MA, Davies GAO, Hellweg HB. Progressive delamination using interface elements. J Compos Mater 1998;32:1246–72.
[47] Wagih A, Maimí P, Blanco N, González E. Scaling effects of composite laminates under out-of-plane loading. Composites A 2019;116:1–12.
[48] Soto A, González E, Maimí P, Turon A, de Aja JS, de la Escalera F. Cohesive zone length of orthotropic materials undergoing delamination. Eng Fract Mech 2016;159:174–88.

[49] Turon A, Camanho P, Costa J, Renart J. Accurate simulation of delamination growth under mixed-mode loading using cohesive elements: Definition of interlaminar strengths and elastic stiffness. Compos Struct 2010;92:1857–64.
[50] Sarrado C, Turon A, Renart J, Urresti I. Assessment of energy dissipation during mixed-mode delamination growth using cohesive zone models. Composites A 2012;43:2128–36.
[51] Carreras L, Renart J, Turon A, Costa J, Bak BLV, Lindgaard E, et al. Experimental data set from a benchmark test of delamination growth with varying crack growth rate and crack front shape under quasi-static and fatigue loading. Mendeley Data, V1; 2018, http://dx.doi.org/10.17632/v7bgzx9gmw.1.
[52] Carreras L, Turon A, Bak B, Lindgaard E, Renart J, de la Escalera FM, et al. A simulation method for fatigue-driven delamination in layered structures involving non-negligible fracture process zones and arbitrarily shaped crack fronts. Composites A 2019;122:107–19.
[53] Maimí P, Renart J, Sarrado C, González E. Characterization of debonding between two different materials with beam like geometries. Eng Fract Mech 2021;247:107661.
[54] Shivakumar KN, Elber W, Illg W. Prediction of impact force and duration due to low-velocity impact on circular composite laminates. J Appl Mech 1985;52:674–80.